# DEPARTURES FROM AXISYMMETRIC MORPHOLOGY AND DYNAMICS IN SPIRAL GALAXIES

David A. Kornreich[1]

Center for Radiophysics and Space Research, Space Sciences Building, Cornell University, Ithaca, NY 14853; kornreic@astrosun.tn.cornell.edu

Martha P. Haynes

Center for Radiophysics and Space Research and National Astronomy and Ionosphere Center,[2] Space Sciences Building, Cornell University, Ithaca, NY 14853; haynes@astrosun.tn.cornell.edu

R. V. E. Lovelace

Department of Astronomy, Space Sciences Building, Cornell University, Ithaca, NY 14853; rvl1@cornell.edu

AND

Liese van Zee[3]

National Radio Astronomy Observatory, P.O. Box O, Socorro, NM 87801;[4] Liese.vanZee@hia.nrc.ca

## ABSTRACT

New H I synthesis data have been obtained for six face-on galaxies with the Very Large Array. These data and reanalyses of three additional data sets make up a sample of nine face-on galaxies analyzed for deviations from axisymmetry in morphology and dynamics. This sample represents a subsample of galaxies already analyzed for morphological symmetry properties in the $R$ band. Four quantitative measures of dynamical nonaxisymmetry are compared with one another and to the quantitative measures of morphological asymmetry in H I and the $R$ band to investigate the relationships between nonaxisymmetric morphology and dynamics. We find no significant relationship between asymmetric morphology and most of the dynamical measures in our sample. A possible relationship is found, however, between morphology and dynamical position angle differences between approaching and receding sides of the galaxy.

*Key words:* galaxies: kinematics and dynamics — galaxies: structure — methods: observational

## 1. INTRODUCTION

Despite the fact that most studies of spiral galaxy dynamics concentrate on understanding the properties of axisymmetric disks, evidence is accumulating that many galaxies lack such overall symmetry. Baldwin, Lynden-Bell, & Sancisi (1980) were the first to seriously examine the asymmetries in galactic disks, pointing out that lopsided galaxies were a common phenomenon not localized to interacting pairs. More recently, the frequency of morphological asymmetry in galactic disks has been quantitatively studied at optical wavelengths. Based on optical morphology, approximately 30% of disk galaxies exhibit significant lopsidedness (Rix & Zaritsky 1995; Kornreich, Hayes, & Lovelace 1998, hereafter KHL). These studies are based on data sets containing some 30 targets each.

Dynamical asymmetry, too, has been examined in large samples of single-dish H I line profiles. Richter & Sancisi (1994), followed by Haynes et al. (1998, hereafter HHMRvZ) with a 104 galaxy sample, examined the symmetry properties of single-dish H I line profiles and determined that as many as ~50% of spiral galaxies show departures from the expected symmetric two-horned profile. Nevertheless, asymmetries in line profiles are ambiguous evidence at best for disturbed dynamics, since they combine both dynamic and spatial information.

Until recently, however, little work had been done to examine the symmetry properties of neutral hydrogen in synthesis data. As a result, the connection between disturbed morphology and disturbed dynamics in field disk galaxies is now only beginning to be seriously studied. Schoenmakers, Franx, & de Zeeuw (1997, hereafter SFdZ) outline a method for measuring small deviations from axisymmetry of the potential of a filled gas disk by breaking down the observed velocity field into its harmonic components. Recently, Swaters et al. (1999, hereafter S3vA) have applied this method to the H I synthesis data of two galaxies, DDO 9 and NGC 4395, where the hallmark of dynamical asymmetry is found to be asymmetry in the rotation curve, in which one side of the curve rises more steeply than the other. H I synthesis observations of several other galaxies, e.g., NGC 3631 (Knapen 1997), 5474 (Rownd, Dickey, & Helou 1994, hereafter RDH), and 7217 (Buta et al. 1995), have also curiously revealed asymmetries or offsets between the optical centers of light and the kinematic centers of the neutral gas. While much evidence exists that many field spirals exhibit nonaxisymmetric morphology and that many field spirals exhibit asymmetric dynamics, the question of whether the two phenomena are correlated or even represent two pictures of a single underlying effect remains open.

Both optical morphology and gas dynamics provide clues as to the overall structure of a galaxy. For instance, Zaritsky & Rix (1997) proposed that optical lopsidedness arises from tidal interactions, minor mergers, or, possibly, gradual accretion. Conselice, Bershady, & Gallagher (2000a), on the other hand, find a correlation between

---

[1] NASA Space Grant Graduate Fellow.

[2] The National Astronomy and Ionosphere Center is operated by Cornell University under a cooperative agreement with the National Science Foundation.

[3] Current address: Herzberg Institute of Astrophysics, 5071 West Saanich Road, Victoria, BC V8X 4M6, Canada.

[4] The National Radio Astronomy Observatory is a facility of the National Science Foundation, operated under a cooperative agreement by Associated Universities, Inc.

optical asymmetry and $B-V$ color and are able to use morphological asymmetry to determine whether starbursts in a given galaxy are likely caused by interactions and mergers. Similarly, the neutral hydrogen dynamics of asymmetric galaxies should be able to distinguish between tidally deformed galaxies and those that are dynamically isolated. For instance, while the strongly optically lopsided galaxy NGC 5474 is well known to be under the tidal influence of its neighbor M101, the disturbed morphologies of the other relatively isolated objects in the KHL sample are not well explained by standard tidal interaction models, which require particular dynamics as well as interactions with (unobserved) nearby companions.

Alternatively, asymmetries may arise from the excitation of unstable, one-armed spiral modes possibly triggered by a past interaction or minor merger (Taga & Iye 1998a, 1998b; Lovelace et al. 1999). Librations of the optical galaxy about the minimum of the gravitational potential might also be set in motion by a previous interaction. As density is dependent on radius in a galaxy, one might expect that the natural modes of a galaxy also depend on radius. The resulting differential oscillation might result in both lopsided appearance and kinematic decoupling from the optical light distribution. An understanding of these modes, if they exist, could provide a direct measure of the dark matter distribution (Jog 1997; SFdZ).

Another type of nonaxisymmetry, warping of galactic disks due to nonplanar motions, has been proposed as an indicator of inclined flattened halo potentials (e.g., Dekel & Shlosman 1983; Toomre 1983), which are required to stabilize the warp against differential precession, as well as observational indicators of massive dark halos (Tubbs & Sanders 1979). Warps may also be due to tidal interactions and accretion and have been reported to be related to noncircular motions, particularly $m = 1$ modes (Weinberg 1998). Although "sloshing" librations in the plane of the galaxy would not imply a correlation between warps and lopsided dynamics, "flapping" librations normal to the galactic plane could contribute to warping.

In this paper, we present H I synthesis data for nine galaxies whose optical asymmetry properties were quantified by KHL. Data obtained from the archives at the Very Large Array (VLA)[5] have been reanalyzed for the galaxies NGC 5474, NGC 5701, and UGC 12732, and new VLA data are presented for the galaxies NGC 991, 1024, 3596, and 4688, UGC 3685, and UGC 6429. These galaxies represent a sample of face-on galaxies selected on the basis of their optical properties.

In § 2, we discuss the acquisition and reduction of the new and archive data for our sample of nine galaxies. In § 3, we analyze the data obtained for deviations from morphological and dynamical axisymmetry and describe methods of determining the magnitudes of such deviations. These quantitative measures are useful for quantifying warps in face-on galaxies and for noncircular motions in more inclined galaxies. We then use the sample to draw correlations between the symmetry parameters of the galaxies to one another and to global H I properties. Finally, in § 4, we present our conclusions in the context of other recent work on galaxy asymmetry.

---

## 2. OBSERVATIONS AND DATA REDUCTION

### 2.1. Target Selection and Observations

The galaxy sample used in this work includes nine galaxies from the sample of KHL. Table 1 summarizes the cataloged data from the Third Reference Catalogue of Bright Galaxies (RC3, de Vaucouleurs et al. 1991) for each of the targets: column (1) lists the NGC or UGC designations of the targets; columns (2) and (3) list the right ascension and declination of the targets in B1950.0 coordinates; column (4) lists the morphological types; column (5) lists the major and minor blue diameters, $D_{25}$ and $d_{25}$; and column (6) lists the face-on blue apparent magnitude corrected for internal and galactic extinction, $B_T^0$.

#### 2.1.1. Original Data Acquisition

Of the optical sample in KHL, the six galaxies NGC 991, 1042, 3596, and 4688, UGC 3685, and UGC 6429 were selected for H I 21 cm synthesis observations based on their apparent degree of asymmetry and position in the sky, such that they could be observed at night during the time scheduled for the CS configuration. As the photometric analysis conducted in KHL had not yet been completed at the time of the target selection, estimates of asymmetry were made by eye. Nighttime observations were preferred to minimize solar interference. The KHL sample was an optically selected sample of disk galaxies chosen on the basis of face-on appearance to permit estimation of the optical morphological asymmetry unencumbered by such factors as absorption by dust and inclination errors. The KHL selection criteria included a small axial ratio, a narrow (typically $W_{50} \lesssim 100$ km s$^{-1}$) velocity width obtained from the private database of Giovanelli & Haynes, known as the Arecibo General Catalog (AGC), and (except for NGC 5474 and NGC 1042) isolation from obvious companions. See KHL for details of the optical target selection.

H I observations of these targets were conducted in 1997 August, 1998 December, and 1999 January with the VLA in its CS configuration. The CS configuration is a modification of the C configuration that provides the resolution of the C configuration while maintaining a sufficient number of short spacings to sample large-scale structure by positioning one or more antennas at D-configuration locations. In 1997, the CS configuration consisted of the standard C configuration with two antennas (from the middle of the east and west arms) relocated at inner D-configuration stations. In 1998 and 1999, one antenna was taken from the middle of the north arm and placed at an inner-D configuration station to provide the requisite short baselines.

Each galaxy was observed for a total of approximately 5.5 hours of on-source integration time in 2AD correlator mode with 127 channels of 12.207 kHz separation after Hanning smoothing. This experimental setup provided a total bandwidth of 1.5625 MHz and, at 1.4 GHz, 2.6 km s$^{-1}$ resolution. Observations were flux and bandpass calibrated by observing flux calibrators for 15 minutes immediately before and after the target observations and phase calibrators for 5 minutes at 30 minute intervals during the target observations.

#### 2.1.2. VLA Archival Data

In addition to the data obtained by us at the VLA, several data sets obtained by other observers were recovered from the VLA data archives for reanalysis. These data sets include observations of the galaxies NGC 5474 (RDH),

TABLE 1

SUMMARY OF GALAXY SAMPLE

| Galaxy (1) | $\alpha$ (B1950.0) (2) | $\delta$ (B1950.0) (3) | Type (RC3) (4) | $D_{25} \times d_{25}$ (arcmin) (5) | $B_T^0$ (6) |
|---|---|---|---|---|---|
| Original Observations | | | | | |
| NGC 991 ........ | 023302.1 | −072234 | SAB(rs)c | 2.7 × 2.4 | 12.30 |
| NGC 1042 ........ | 023756.3 | −083850 | SAB(rs)cd | 4.7 × 3.6 | 11.38 |
| UGC 3685 ....... | 070433.1 | +614029 | SB(rs)b | 3.3 × 2.8 | 12.30 |
| NGC 3596 ....... | 111227.9 | +150338 | SAB(rs)c | 4.0 × 3.8 | 11.67 |
| UGC 6429 ....... | 112225.1 | +640011 | SA(rs)c | 2.1 × 1.7 | 13.63 |
| NGC 4688 ....... | 124513.8 | +043558 | SB(s)cd | 3.2 × 2.8 | 12.47 |
| Archive Data | | | | | |
| NGC 5474 ....... | 140314.6 | +535403 | SA(s)cd pec | 4.8 × 4.3 | 11.27 |
| NGC 5701 ....... | 143641.5 | +053450 | (R)SB(rs)0/a | 4.3 × 4.1 | 11.69 |
| UGC 12732...... | 233808.8 | +255727 | Sm | 3.0 × 2.8 | 13.55 |

NGC 5701 (observed by S. E. Schneider in 1986), and UGC 12732 (Schulman et al. 1997). These targets were chosen because each was analyzed for optical morphological asymmetry as part of the KHL sample and because VLA archive H I line data of sufficient sensitivity (about $10^{20}$ cm$^{-2}$) and spectral resolution (less than 15 km s$^{-1}$) for the current analysis existed for them. The archival data were retrieved as raw UV visibility data and reduced by the same methods as were used for our original observations. The raw data sets for NGC 5701 and UGC 12732 were Hanning smoothed on-line by their observers; that of NGC 5474 was not.

An observational summary of the nine VLA data sets in the total sample is presented in Table 2. Column (1) lists the NGC or UGC designation of the target. Column (2) lists the VLA configuration in which the data were obtained. Column (3) lists the date of the observation. Column (4) lists the observer or paper in which the observation was reported. Column (5) lists the total on-source integration time in minutes. Column (6) lists the total bandwidth in megahertz. Column (7) lists the channel separation in kilometers per second. Column (8) lists the total number of channels in the data set. Column (9) lists the synthesized clean beam size in our naturally weighted maps in arcseconds. Column (10) lists the rms noise $\sigma$ observed in the line-free channels in millijanskys per beam.

The archival data sets were obtained between early 1983 and 1993, with the earlier data sets consisting of a small number of channels in the D configuration. While we expected to improve marginally upon the previous data reduction for these archival data sets, we were surprised to find that because of the exponential improvement in computer technology since that time, the reanalysis of these data yielded a remarkable improvement over the initial analyses. By cleaning the data to deeper levels than was possible in the past, we were able to measure H I column densities up to almost an order of magnitude fainter than those previously reported for the same data sets. As an example, we were able to iteratively clean the UV data for NGC 5474 for 200,000 iterations, down to the 1 $\sigma$ theoretical noise level, as compared with the 500 iterations reported by RDH. Our reanalysis was thus able to trace the H I to a 1 $\sigma$ column density of $6 \times 10^{18}$ cm$^{-2}$ channel$^{-1}$, compared with the $1.2 \times 10^{19}$ cm$^{-2}$ channel$^{-1}$ quoted in RDH, an improve-

ment of about one-half an order of magnitude with the same data set. This greater sensitivity allowed us to uncover the very peculiar outer dynamics of this galaxy not observed by RDH, structure which is of dynamical importance. As expected, such large gains in sensitivity were most pronounced from the earlier data sets and of less importance for later ones.

## 2.2. *UV Processing and Data Analysis*

Reduction of the visibility data was conducted using the Astronomical Image Processing System (AIPS; Napier, Thompson, & Ekers 1983).[6] Data were examined via the program TVFLG, in which poor-quality UV data were identified and flagged. Following the flagging procedure, a linear interpolation of bandpass calibrations obtained from the phase calibrators for each galaxy was obtained and applied to the target data.

The continuum was then subtracted from each data set using the program UVLIN (Cornwell, Uson, & Haddad 1992), which subtracts continuum emission from all channels, based on a linear fit of the visibilities in a given number of line-free channels, as selected by manual inspection. The total number of line-free channels used varied according to the data set, but they typically numbered about 30 for originally acquired data and 10 for archive data. The UV data were then transformed to the $(x, y)$-plane using the program IMAGR.

At this point in the calibration, it was discovered that the cataloged declination of the phase calibrator used with the UGC 6429 data set was incorrect by 1′. This had the effect of producing incorrect coordinates in the $(x, y)$ data cubes. This problem was solved by identifying continuum sources observed in the raw image with sources cataloged in the NRAO VLA Sky Survey (Condon et al. 1998) and performing astrometry on these sources.

For each galaxy, data cubes were constructed using both natural and robust weighting. We present in Figure 1 the data cubes in the form of channel maps derived by natural weighting, because natural weighting appeared to strike the best balance between the signal-to-noise ratio and

---

[6] AIPS is distributed by the National Radio Astronomy Observatory.

TABLE 2
Observational Summary

| Galaxy (1) | Configuration (2) | Date (3) | Reference (4) | $t_{int}$ (min) (5) | $W_{band}$ (MHz) (6) | $W_{chan}$ (km s$^{-1}$) (7) | $N_{chan}$ (8) | Beam (arcsec) (9) | $\sigma$ (mJy beam$^{-1}$) (10) |
|---|---|---|---|---|---|---|---|---|---|
| NGC 991 ........ | CS | 1997 Aug | This work | 381 | 1.5625 | 2.60 | 127 | 25 × 20 | 0.8 |
| NGC 1042 ....... | CS | 1997 Aug | This work | 380 | 1.5625 | 2.60 | 127 | 23 × 18 | 0.8 |
| UGC 3685 ....... | CS | 1997 Aug | This work | 380.5 | 1.5625 | 2.60 | 127 | 19 × 18 | 0.7 |
| NGC 3596 ....... | CS | 1999 Jan | This work | 503.5 | 1.5625 | 2.60 | 127 | 19 × 18 | 0.7 |
| UGC 6429 ....... | CS | 1999 Jan | This work | 377 | 1.5625 | 2.64 | 127 | 20 × 16 | 0.6 |
| NGC 4688 ....... | CS | 1998 Dec | This work | 370.5 | 1.5625 | 2.59 | 127 | 21 × 18 | 0.8 |
| NGC 5474 ....... | D | 1983 Jul | Rownd et al. 1994 | 287.5 | 3.125 | 2.58 | 31 | 54 × 51 | 2.2 |
| NGC 5701 ....... | D | 1987 Apr | S. E. Schneider | 750.5 | 3.125 | 10.41 | 31 | 70 × 63 | 1.3 |
| UGC 12732...... | D | 1992 Aug | Schulman et al. 1997 | 660 | 3.125 | 10.36 | 63 | 54 × 53 | 0.4 |

resolution. This figure presents the channels containing signals for each galaxy, bracketed by several noise channels. The channel velocity for each panel is given at upper left. For most of the targets, which had emission in a large number of channels, only every other channel is depicted. For UGC 6429 and NGC 4688, which were detected in a smaller number of channels, every channel containing a signal is shown.

Following this standard visibility reduction, the data image cubes were transferred for further reduction in the GIPSY environment (van der Hulst et al. 1992)[7]. Copies of the data cubes were then smoothed to provide easier separation of regions with signals from regions with no signals. Data in these copies were cropped at the 3 $\sigma$ level. The cropped regions were then mapped back to the

---

[7] For GIPSY, the Groningen Image Processing System, see http://thales.astro.rug.nl/~gipsy/.
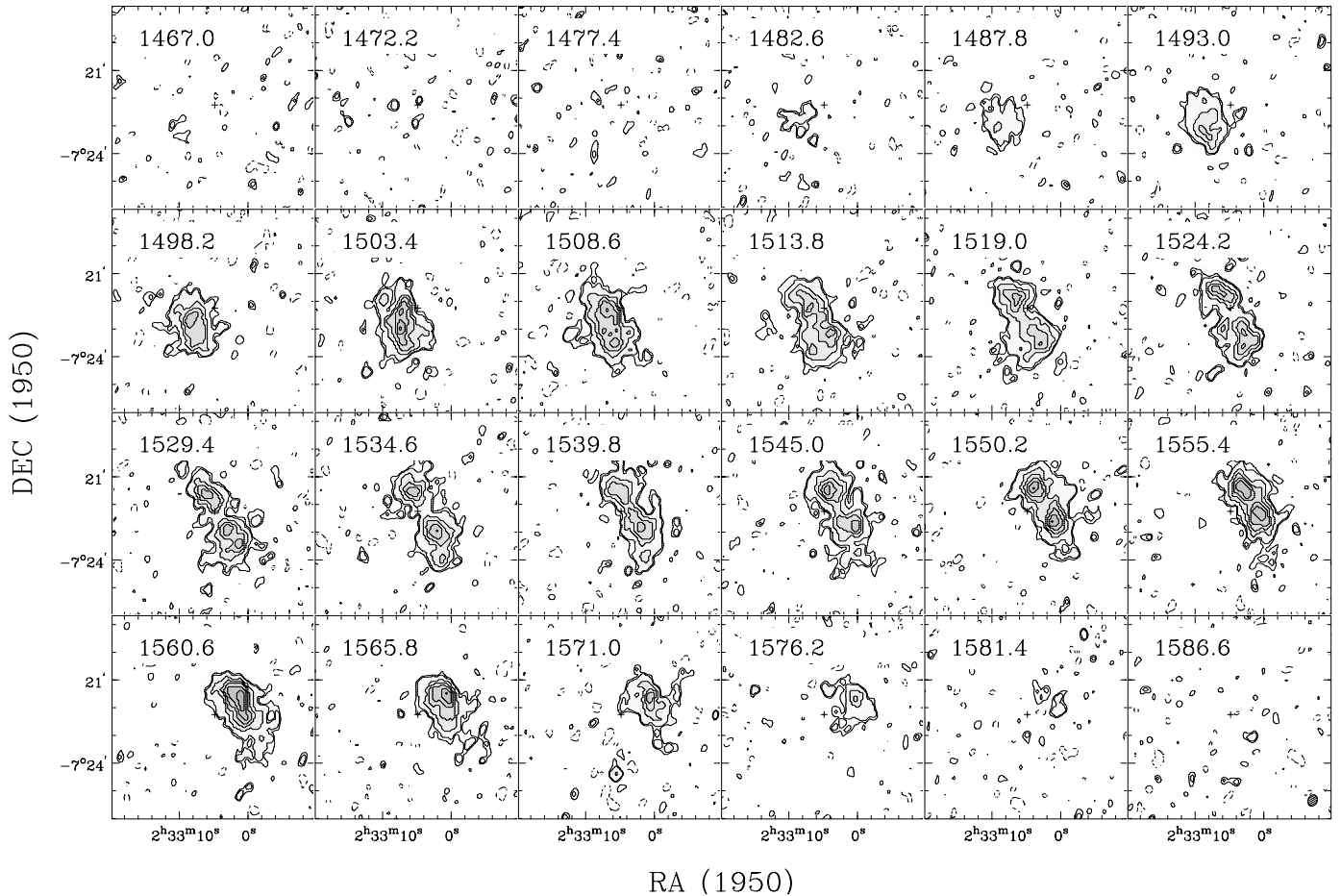


Fig. 1a

Fig. 1.—Channel maps for each of the six new data sets in the sample: (a) NGC 991, (b) NGC 1042, (c) UGC 3685, (d) NGC 3596, (e) UGC 6429, and (f) NGC 3688. Channel velocity is given in each panel, and contours are at the $(-2, 2, 3, 6, 9, \ldots)$ $\sigma$ levels, where $\sigma$ is as listed in Table 2. Gray scales are at the $(6, 12, 18, \ldots)$ $\sigma$ levels.
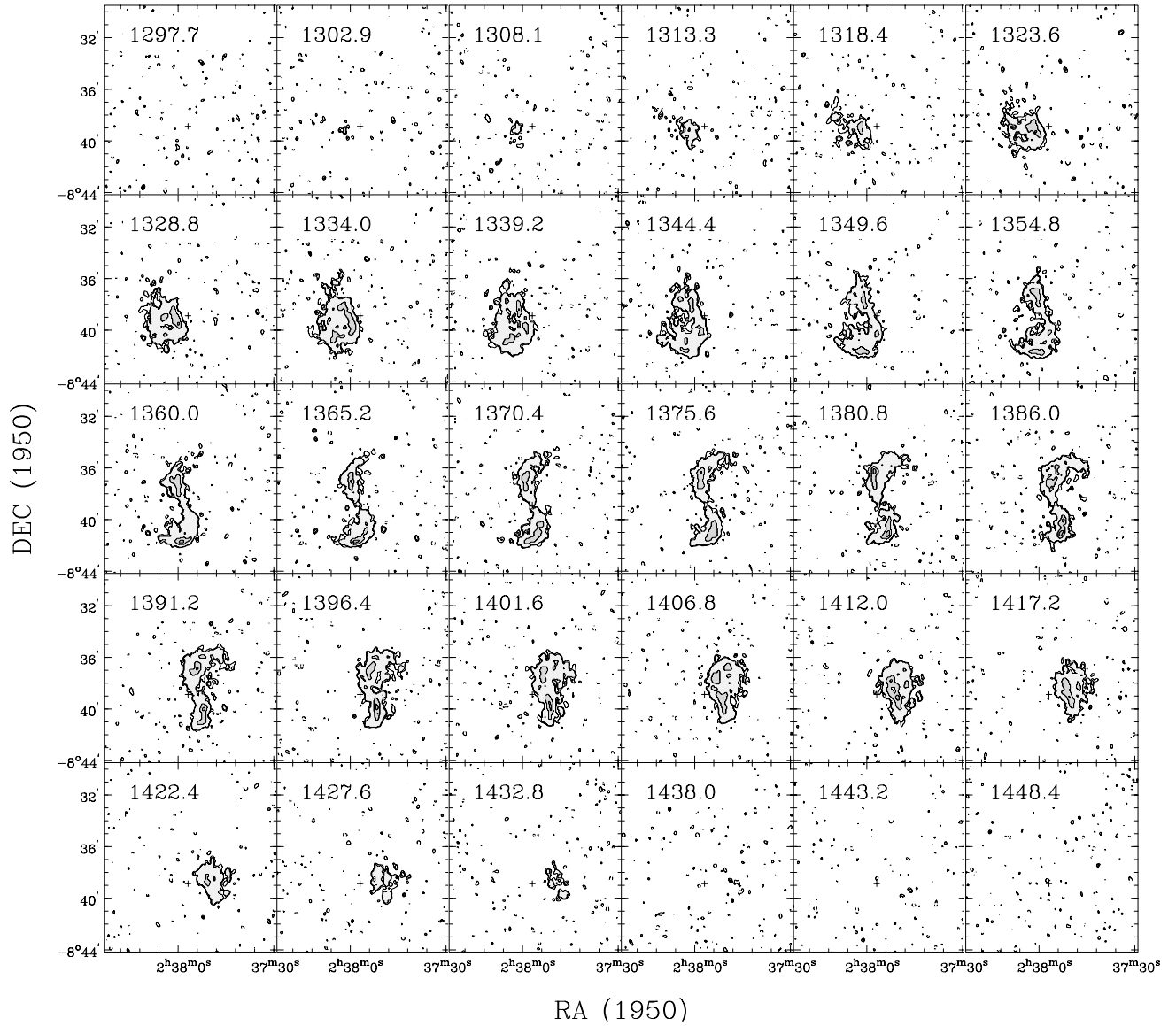
DEC (1950)

RA (1950)

Fig. 1b

unsmoothed cubes, which then consisted only of regions containing signals. Following correction for primary beam, these regions were integrated along the velocity axis into zeroth, first, and second moments of the flux, thus creating three spatial maps, representing the H I flux, bulk motion, and velocity dispersion, respectively. To eliminate spurious noise peaks during this integration, a "windowing" function was used so that only peaks seen in two or more consecutive channels were included in the integration. The H I flux was then scaled to the column density $N$ of the gas, assuming optically thin H I, via the relation

$$N = 1.10297 \times 10^{24} \text{ cm}^{-2} \int \frac{S}{ab} \left(1 + \frac{v}{c}\right)^2 dv , \quad (1)$$

where $S$ is the total flux density in Janskys per beam and $a$ and $b$ are the major and minor FWHM axes of the Gaussian beam in arcseconds.

Following construction of the moment maps, simulated single-dish line profiles for each galaxy were obtained by

integrating the data cubes over the spatial axes. Total integrated flux measurements were obtained by integrating the line profiles along the velocity axis. They were then compared with single-dish data obtained from various sources. These single-dish data were corrected for pointing errors and beam smearing following the two-Gaussian distribution model of Hewitt, Haynes, & Giovanelli (1983), with the Gaussian parameters derived from the synthesis data obtained here by fitting a double Gaussian to the moment-zero maps. The comparison of synthesis with corrected single-dish flux is presented as part of Table 3. Following the discussion of Hewitt et al. (1983), we expect between 15% and 20% uncertainty in the derived corrected flux. In general, there is agreement within the errors between the total flux measurements derived here and the single-dish data.

The first-order moment maps were used to obtain a kinematic model of the galaxies by iteratively applying the standard GIPSY routine ROTCUR (Begeman 1989). This routine divides the galaxy into a number of rings and fits a
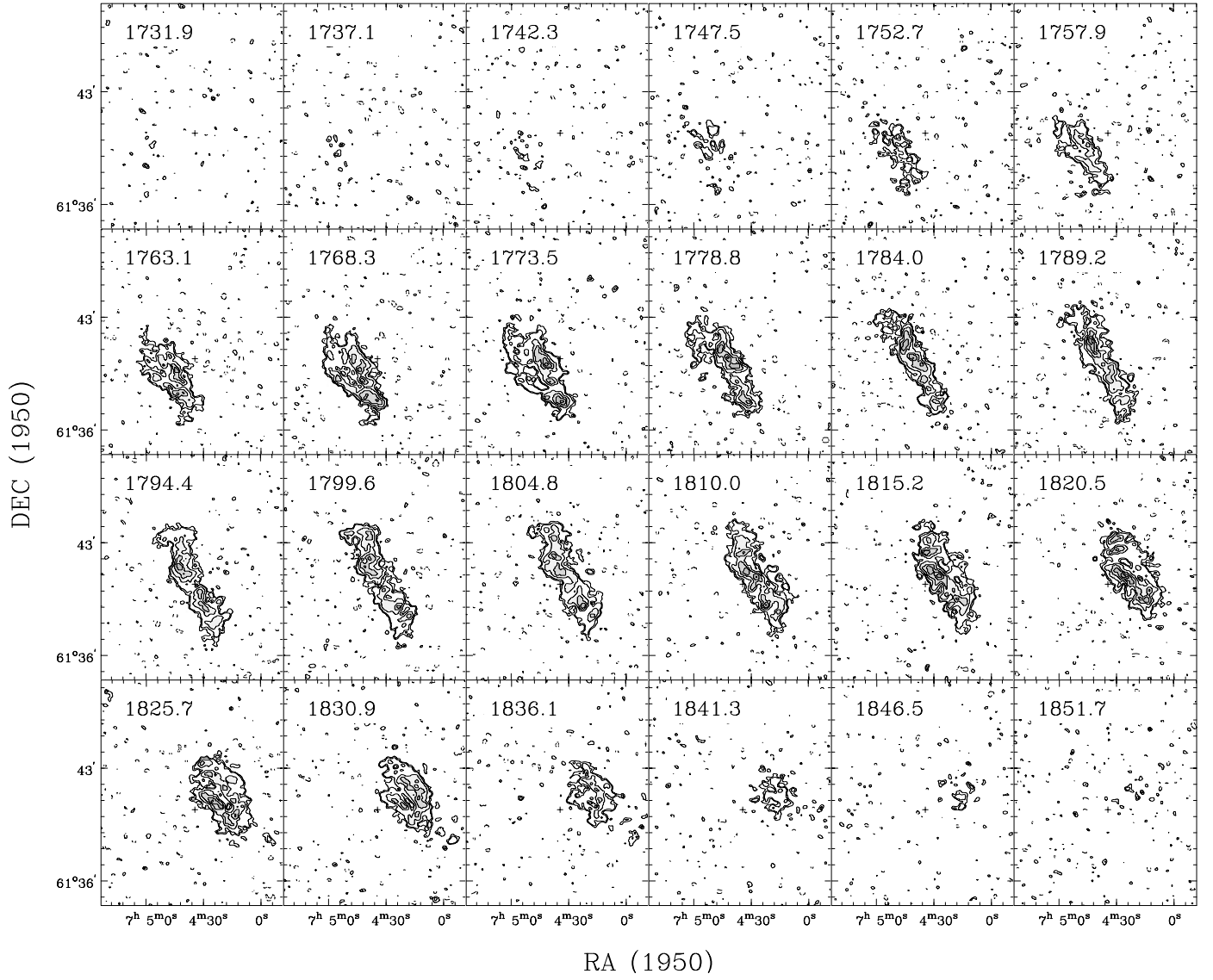
1731.9 1737.1 1742.3 1747.5 1752.7 1757.9

1763.1 1768.3 1773.5 1778.8 1784.0 1789.2

1794.4 1799.6 1804.8 1810.0 1815.2 1820.5

1825.7 1830.9 1836.1 1841.3 1846.5 1851.7

43'

61°36'

DEC (1950)

$7^h 5^m 0^s$  $4^m 30^s$  $0^s$

RA (1950)

Fig. 1c

TABLE 3

GLOBAL H I PROPERTIES

| Galaxy (1) | $F_{\rm VLA}$ (Jy km s$^{-1}$) (2) | $F_{\rm SD}$ (Jy km s$^{-1}$) (3) | $W_{20}$ (km s$^{-1}$) (4) | $V_{\rm HI}$ (km s$^{-1}$) (5) | $D_{\rm HI}/D_{25}$ (6) | $V_{\rm rot} \sin i$ (km s$^{-1}$) (7) | Dist. (Mpc) (8) | $M_{\rm HI}$ ($10^9\ M_\odot$) (9) | $M_{\rm HI}/L_B$ ($M_\odot/L_\odot$) (10) |
|---|---|---|---|---|---|---|---|---|---|
| NGC 991 ........ | 21 | 21[a] | 91 | 1531 | 1.9 | 33.0 | 20 | 2.0 | 0.27 |
| NGC 1042 ....... | 55 | 56[a] | 116 | 1372 | 1.7 | 43.7 | 20 | 5.2 | 0.30 |
| UGC 3685 ....... | 43 | 55[a] | 97 | 1796 | 2.1 | 36.8 | 30 | 9.1 | 0.54 |
| NGC 3596 ....... | 29 | 33[b] | 127 | 1193 | 1.1 | 51.7 | 14 | 1.3 | 0.20 |
| UGC 6429 ....... | 10 | 11[c] | 69 | 3727 | 1.5 | 23.3 | 75 | 13 | 0.42 |
| NGC 4688 ....... | 28 | 35[a] | 60 | 984 | 1.8 | 18.1 | 17 | 1.9 | 0.41 |
| NGC 5474 ....... | 78 | 120[a] | 60 | 277 | 1.9 | 8.2 | 7 | 0.9 | 0.40 |
| NGC 5701 ....... | 58 | 63[b] | 139 | 1509 | 2.6 | 57.1 | 26 | 9.3 | 0.42 |
| UGC 12732...... | 79 | 79[a] | 139 | 746 | 3.1 | 54.6 | 15 | 4.2 | 3.2 |

[a] Fisher & Tully 1981.
[b] HHMRvZ.
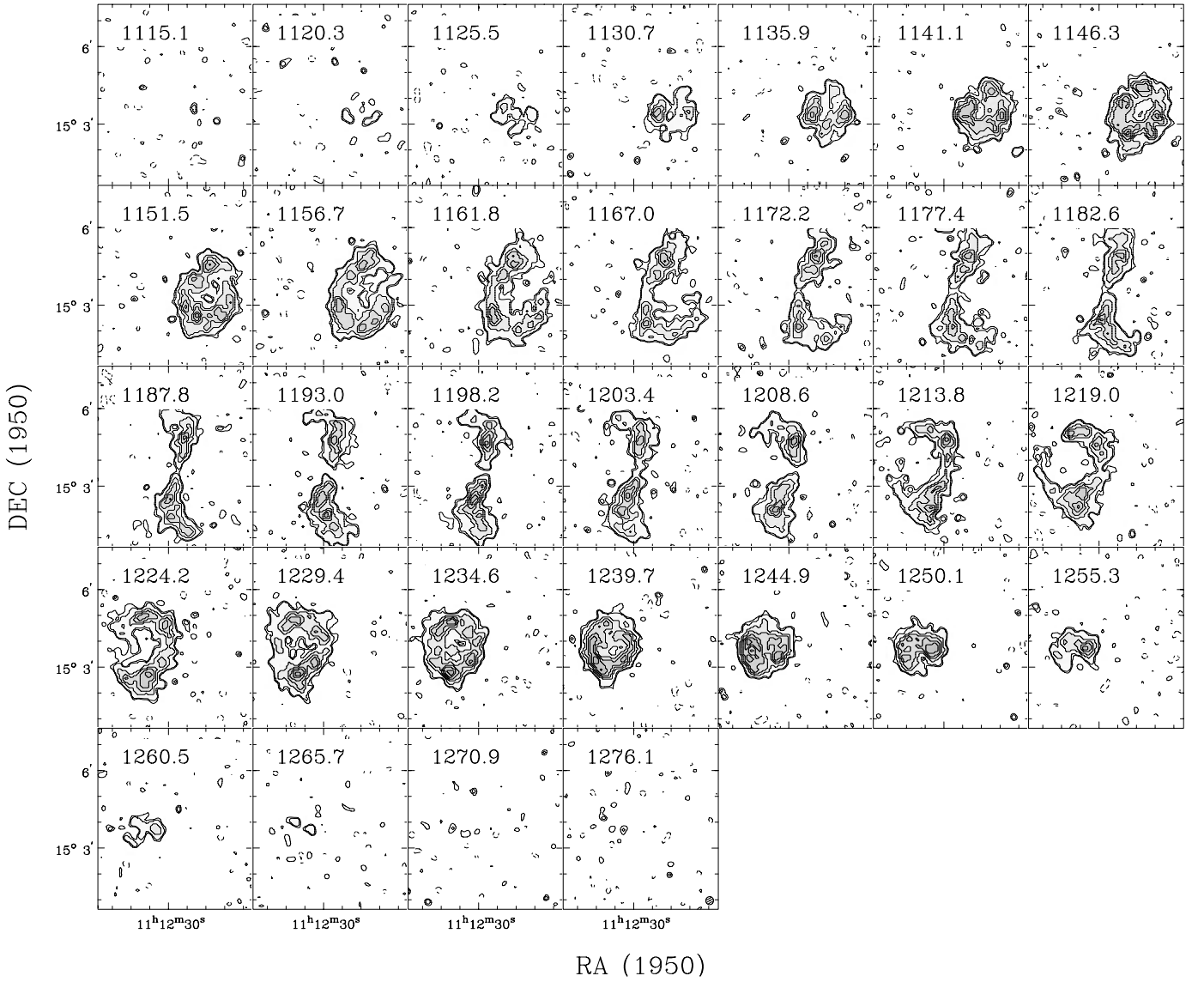[c] Staveley-Smith & Davies 1988.

FIG. 1d

function

$$V(x, y) = V_{\text{sys}} + V_{\text{rot}} \cos \theta \sin i , \qquad (2)$$

where

$$\cos \theta = \frac{-(x - x_0) \sin \Gamma + (y - y_0) \cos \Gamma}{r} , \qquad (3)$$

to the velocity field in each ring, allowing the systematic velocity, $V_{\text{sys}}$, the rotation velocity, $V_{\text{rot}}$, inclination, $i$, position angle, $\Gamma$, and kinematic center, $(x_0, y_0)$, to vary.

Because of the face-on aspect of the target galaxies, adequate kinematic solutions could be found, but they were spread over a large area of parameter space. Specifically, although $V_{\text{rot}} \sin i$ remained well constrained for each ring, changes in $V_{\text{rot}}$ and $i$ were found to be interchangeable with little effect on the quality of fit in the model function. The result was often that the algorithm produced unphysical values of $V_{\text{rot}}$ with wildly varying inclinations if all parameters were allowed to vary independently. For this reason,

the ROTCUR model was applied iteratively to the data, alternately holding $V_{\text{rot}}(r)$, $i(r)$, and $(x_0, y_0)$ fixed. We present rotation curves and all subsequent analysis in terms of $V_{\text{rot}} \sin i$. We caution, therefore, that variations in the $V_{\text{rot}} \sin i$ $(r)$ curves we present may represent actual changes in the rotation velocities of the galaxies, changes in the galaxies' inclinations, or a combination of both. Inability to constrain $V_{\text{rot}}(r)$ further also precluded the construction of reliable model velocity fields that could reasonably be expected to reproduce the potentials of the galaxies. Once the tilted-ring fit was applied iteratively to the entire galaxy to obtain initial values of the parameters, the model was separately fitted to each half of the galaxy, so that $V_{\text{rot}} \sin i$ $(r)$ and position angles could be determined for each side independently.

Position-velocity diagrams for one beam width along the major axis of each data set were then obtained. To construct the position-velocity diagrams, slices of the data cubes were taken through the kinematic centers obtained in the model fitting. Each slice was a strip of data whose
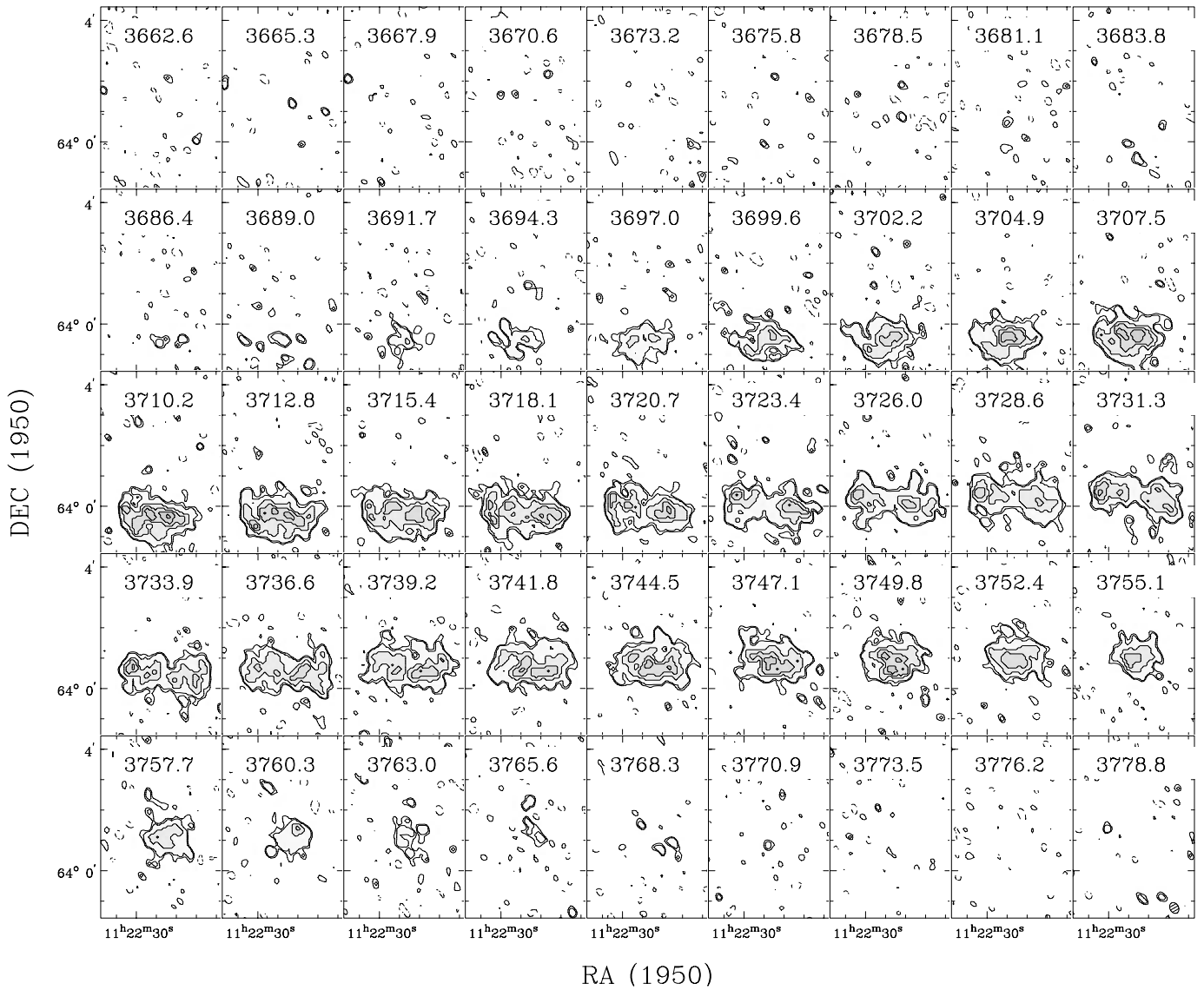
FIG. 1e

spatial length was the total detected extent of the galaxy, whose spatial width was the width of a beam, and whose frequency depth was the depth of the cube. The spatial position angle of the slice was determined by averaging the model position angles over radii $r \leq R_{25}$. Data were then averaged over the width of the slice to produce the position-velocity diagrams.

Distances to most of the sample galaxies were determined using a nonlinear Virgocentric infall model with an infall flow velocity of the Local Group of 230 km s$^{-1}$, Hubble parameter $H_0 = 74$ km s$^{-1}$ Mpc$^{-1}$, distance to Virgo of 16.6 Mpc, and the mean overdensity of the Virgo Cluster compared with the ambient density of $\rho_{\mathrm{Virgo}}/\rho_0 = 2$. Our model uses these parameters to solve for the velocity field of the local universe and then to find the possible distances of individual galaxies by finding the roots of the difference of the velocity with respect to the Local Group (derived from the heliocentric velocity by the method of Mould, Aaronson, & Huchra 1980) and the velocity found for a given distance. This is done by using the numerical recipes (Press

et al. 1986) routine ZBRAK to determine the bounds of the regions surrounding each root, which are then used to solve for the roots themselves.

This model yields multiple distances for galaxies in the triple-valued region close to the Virgo Cluster. Distances of 12, 14, and 24 Mpc were obtained for NGC 3596, and 7, 17, and 22 Mpc for NGC 4688. Here, we have taken the value of 14 Mpc for NGC 3596, based on the distance modulus of 31.41 found by Bottinelli et al. (1985) using the Tully-Fisher relation of H I line width and B-band luminosity. We have taken a distance of 17 Mpc for NGC 4688 based on a study of supernovae by Gaskell (1992), in which a distance of 17 Mpc yields a peak luminosity of SN 1966B commensurate with other Type II-L supernovae. Following RDH, the distance to NGC 5474 of 7 Mpc was taken directly from Sandage & Tammann (1974), where distances to galaxies in the M101 system were found by measuring the angular sizes of H II regions. We have also adopted a value of 20 Mpc for NGC 991, equal to that of NGC 1042, because both galaxies are found by Garcia (1993) to be members of LGG 71,
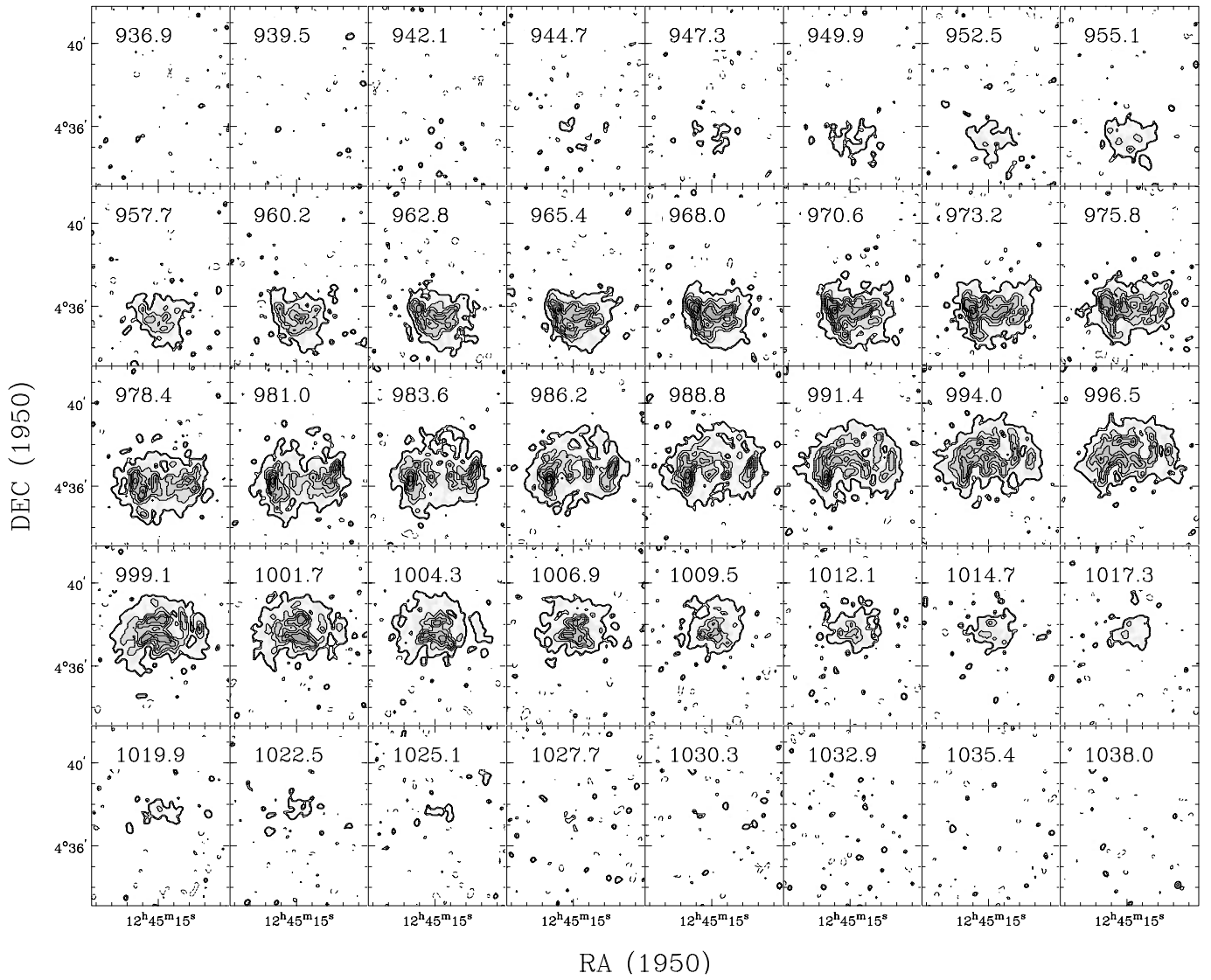
FIG. 1*f*

a loose group of galaxies that includes the NGC 1052 group.

The global H I properties derived from the analysis are presented in Table 3. Column (1) lists the NGC or UGC designation of the target. Column (2) lists the integrated total flux observed at the VLA, $F_{\rm VLA}$, in Jy km s$^{-1}$. Column (3) lists the single-dish flux, $F_{\rm SD}$, in Jy km s$^{-1}$, corrected for pointing errors and beam dilution as described earlier in this section and with an associated reference for the uncorrected flux measurement. Column (4) lists the full width of the H I line profile measured at 20% of the peak flux, $W_{20}$, in kilometers per second. Column (5) lists the systematic velocity $V_{\rm HI}$ of the target in kilometers per second, obtained from tilted-ring modeling of the data with typical errors of $\pm 5$ km s$^{-1}$. Column (6) lists the ratio of the H I to optical diameters, $D_{\rm HI}/D_{25}$, where $D_{\rm HI}$ is measured at a surface density of 1 $M_\odot$ pc$^{-2}$. Column (7) lists the observed value of $V_{\rm rot} \sin i$ averaged over the flat part of the curve. Column (8) lists the distance to the target, in megaparsecs, obtained from the Virgocentric infall mode. Column (9) lists total H I mass observed at the VLA, obtained from the flux density

via the relation

$$M_{\rm HI} = 2.36 \times 10^5 \ M_\odot \left(\frac{D^2}{1 \ {\rm Mpc}^2}\right) \int \frac{S_v}{1 \ {\rm Jy}} \frac{dv}{1 \ {\rm km \ s}^{-1}} \ , \quad (4)$$

where $D$ is the distance to the galaxy and $S_v$ is the H I flux density in Janskys. Column (10) lists the ratio $M_{\rm HI}/L_B$ of H I mass to blue luminosity, where the luminosity is derived from $B_T^0$.

### 2.3. Qualitative Features of the Target Objects

General comments regarding the gas morphology and dynamics of each target are discussed in this subsection. The text describing each galaxy is accompanied by a figure presenting, in the top two panels, the H I column density contours overlaid on the optical image of the galaxy obtained by KHL and a gray-scale map of the H I column density itself. Noise in the column density maps differs from pixel to pixel because of the windowing function and was corrected for noise correlations among Hanning-smoothed channels following the discussion of Verheijen (1997). The

noise in a given pixel is

$$\sigma^l = \frac{4}{\sqrt{6}} \left[ \left( N - \frac{3}{4} \right) + N^2 \mathcal{N}^2 \right]^{1/2} \sigma^h , \qquad (5)$$

where $N$ is the number of adjacent Hanning-smoothed channels that contributed to the pixel, $\sigma^h$ is the noise in a single channel, and

$$\mathcal{N} \equiv \sqrt{\frac{[N_1 - (3/4)]}{4N_1^2} + \frac{[N_2 - (3/4)]}{4N_2^2}} \qquad (6)$$

is a factor representing the noise contributed by subtracting the first $N_1$ and last $N_2$, line-free channels from the cube. The average pixel value for all pixels with signal-to-noise ratio $2.75 < S/N < 3.25$ was taken to define the 3 $\sigma$ level for the map. Column density contours in the maps are selected for each galaxy individually, based primarily on clarity of presentation, and the H I gray scales are continuous and linear.

To produce the optical overlays, astrometry was performed for each of the $R$-band images obtained in KHL corresponding to the VLA target galaxies, based on star positions obtained from the *HST* Guide Star Catalog (Lasker et al. 1992). This also allowed morphological asymmetry measurements to be made with respect to the position of the galaxies' optical nuclei.

The center left panels exhibit the position-velocity diagram along the H I dynamical major axis, as determined by averaging over the position angles for all radii inside $R_{25}$. The position angle is given at the top of the plot, and the position axis is measured in arcminutes north from the dynamical center. Vertical lines in the position-velocity diagram indicate $R_{25}$. Graininess of the archive data is due to the large channel widths and the small number of channels in these sets, which make the corresponding diagrams data sparse.

The center left panel is a gray-scale representation of the H I velocity distribution with gray-scale steps equal to the contours. Again, the contours and gray scales are chosen individually for each galaxy, based on clarity of presentation. Dark gray scales represent the receding side of the galaxy; lighter gray scales, the approaching side. Values for selected contours are presented in kilometers per second. Overlaid on the gray-scale moment panels are circles of radius $R_{25}$ centered on the center of light of the optical galaxies, except for NGC 5474, where the center of light is so displaced from both the dynamical center and the center of the outer optical isophotes that the dynamical center is used. We have elected to show circles here, although the RC3 indicates some elongation, as evident from Table 1, because of ambiguity in extracting asymmetry versus inclination for face-on objects.

Finally, the bottom two panels present the integrated H I line profile and $V_{rot} \sin i(r)$ for the galaxy. This latter diagram presents the data for the line-of-sight rotation velocity $V_{rot} \sin i$ (in kilometers per second) and position angle (degrees east of north) from the tilted-ring–fitting algorithm as a function of radius in arcseconds. The error values given are the numerical errors in the fitting algorithm; we estimate that systematic errors are on the order of 2 times as large. The data for the approaching side (*circles and solid lines*) and the receding side (*triangles and dashed lines*) are presented superposed. It is important to note that the ordinate of the rotation plot does not start at zero;

because of beam smearing, we cannot trace the rotation close to the center. The differences between values for the approaching and receding sides would be washed out with an increased scale.

### 2.3.1. *NGC 991*

NGC 991 (Fig. 2) is a flocculent SBc galaxy whose northwestern spiral arms extend twice as far from the nucleus as do the visible southeastern arms. Since the optical flux of the flocculent structures northwest of the nucleus is greater than that to the southeast, it is classified as asymmetric by KHL. The bar is elongated in the east-west direction. The detected neutral hydrogen extends to 1.5 times the optical radius. A neutral hydrogen disk of $1.2 \times 10^{21}$ cm$^{-2}$ coexists with the optical disk, except for a gap over the underluminous southern disk, which has average H I column density $8.5 \times 10^{20}$ cm$^{-2}$. This gap appears in a partial H I ring with two flux maxima at a radius of 1' (6.4 kpc). The outer H I disk is morphologically symmetric. According to Garcia (1993), the nearest neighbor to NGC 991 in LGG 71 is NGC 1022, 34' (198 kpc at the adopted distance of 20 Mpc) to the northeast.

The H I dynamics of NGC 991 are relatively undisturbed within the optical radius, as illustrated in the position-velocity diagram (see Fig. 2, *center left*), but certain non-axisymmetric dynamical features are evident in the outer disk. Closed contours on the east side of the major axis indicate a possible warp in the disk. Strong twisting of the minor axis velocity contours analogous to the S-shaped velocity contours of NGC 5474 (see § 2.3.7) is also present in NGC 991. The same phenomenon can also be seen in the channel maps as an area of enhanced flux to the east of the galaxy at 1513.8 and 1508.6 km s$^{-1}$. This indicates either a severely warped disk or strong streaming motions through an outer spiral arm. The dynamical center of the velocity distribution is consistent with the $R$-band center of light of the galaxy, but the dynamics exhibit a 40° maximum shift in position angle from approaching to receding side for the same radius, as a result of the detected S-shaped velocity contours. The synthesized line profile is asymmetric, with decreasing flux toward the approaching side.

### 2.3.2. *NGC 1042*

NGC 1042 was first mapped in H I by van Gorkom et al. (1986), whose primary purpose was to obtain H I synthesis data for the elliptical NGC 1052 and its companions, which include NGC 1042, some 15' (87 kpc at the adopted distance of 20 Mpc) southwest of NGC 1052. They point out that the neutral gas in NGC 1042 is asymmetric in the direction of NGC 1052, suggesting a tidal interaction. Because these data were collected with only 18 antennas, yielding a synthesized beam of $60'' \times 60''$ at a velocity resolution (41 km s$^{-1}$) more suited to the inclined galaxy NGC 1052, it was decided that newer data were required to better constrain the dynamical parameters. These new data we present here.

NGC 1042 (Fig. 3) is a nearby asymmetric spiral galaxy whose eastern spiral arm contains many active H II regions, but whose western spiral arm is underluminous. Although the total H I flux agrees with previous observations, the H I mass derived from our data is larger by a factor of 2 than that reported by van Gorkom et al. (1986 and references therein), because of the difference in adopted distances.
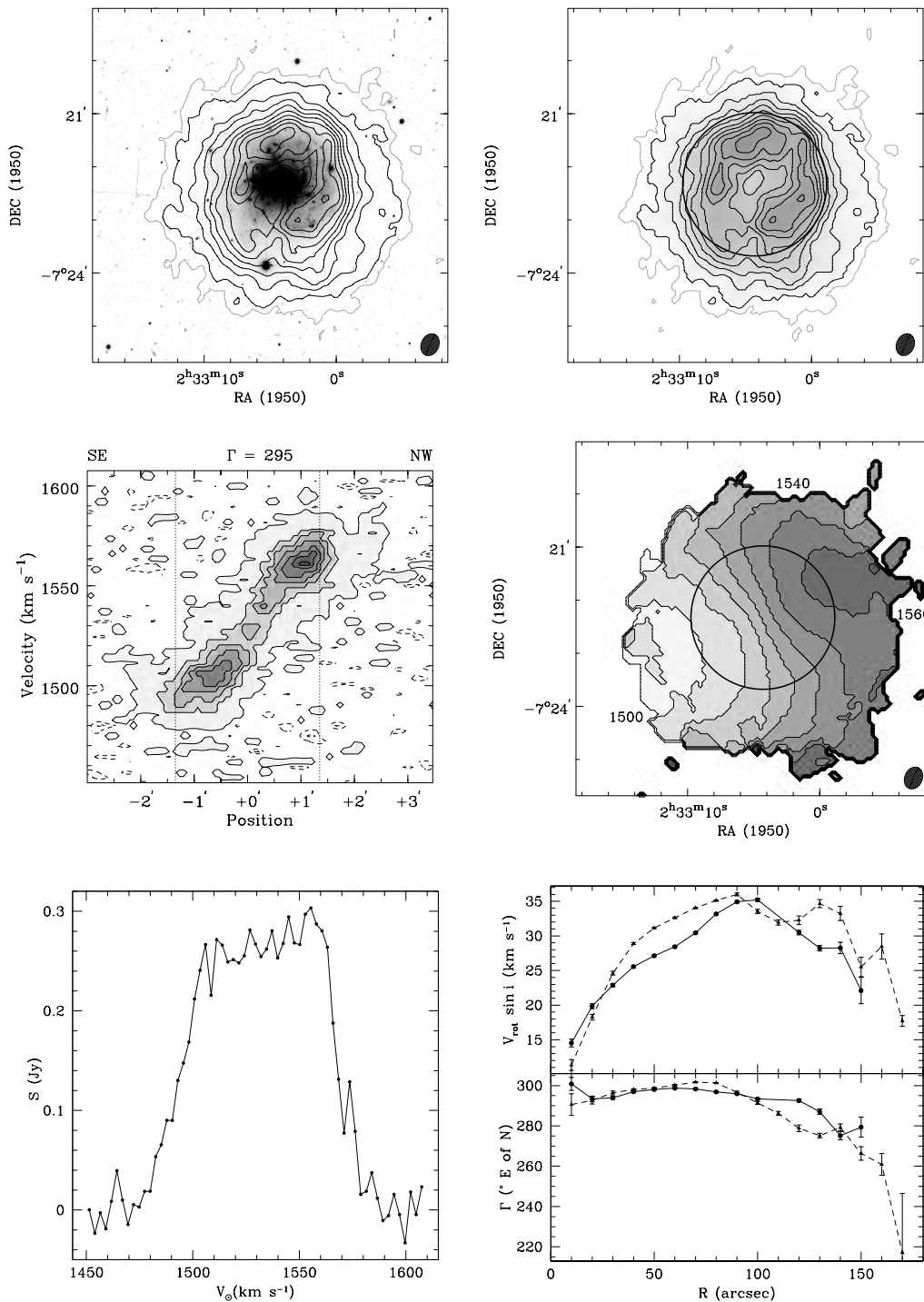
FIG. 2.—VLA H I synthesis results for NGC 991. *Top left*: H I column density contours detected at the VLA, with light gray contour at $3.4 \times 10^{19}$ cm$^{-2}$ and solid contours at $(10.2, 23.8, 37.4, 51.0, \ldots) \times 10^{19}$ cm$^{-2}$, overlaid on the *R*-band image obtained by KHL. The first solid contour represents the 3 $\sigma$ noise level. *Top right*: Same H I column density contours as at top left, but plotted over a linear gray-scale column density map. The circle has diameter $D_{25}$ and is centered on the *R*-band center of light of the galaxy. *Center left*: Position-velocity diagram obtained from the H I data cube. The slice was made along the dynamical major axis $\Gamma = 295°$ determined by averaging the dynamical position angle over radii $r < R_{25}$. The *x*-axis indicates arcminutes northwest of the dynamical center, and the vertical lines identify $R_{25}$. *Center right*: H I observed velocity field with contours and gray scales from 1490 (east; *light shading*) to 1570 km s$^{-1}$ (west; *dark shading*) in increments of 10 km s$^{-1}$. The 1500, 1540, and 1580 km s$^{-1}$ contours are identified. The circle has diameter $D_{25}$ and is centered on the *R*-band center of light of the galaxy. *Bottom left*: Synthesized H I line profile obtained by integrating the data cube along both spatial axes. *Bottom right*: Rotation $V_{rot} \sin i$ and dynamical major axis position angle $\Gamma$ as a function of radius in arcseconds, obtained from the tilted-ring model. The data for the approaching side (*circles and solid lines*) and the receding side (*triangles and dashed lines*) are presented superposed.

The H I morphology of this galaxy is unremarkable inside the optical radius, with the H I column density following the pattern of the dominant spiral arms outside the central H I hole. Asymmetry in the outer regions, however, is clear. The column density drop-off toward the northeast is far more gradual than the precipitous drop-off to the southwest, giving the galaxy the appearance of compression on the southwestern "forward" edge, as if traveling parallel to its
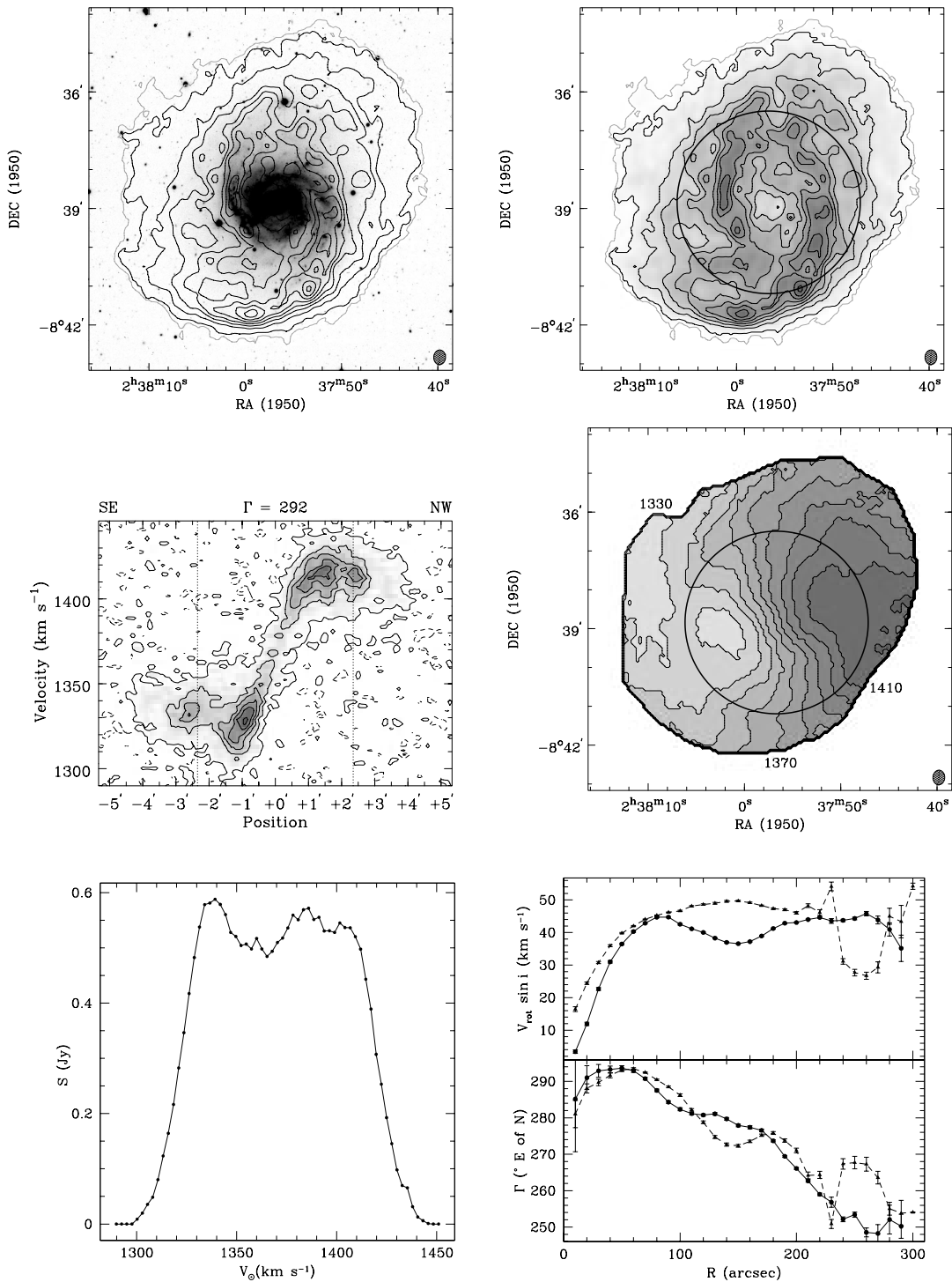
FIG. 3.—Same as Fig. 2, but for NGC 1042. Light gray H I column density contours are at $2.6 \times 10^{19}$ cm$^{-2}$ and solid contours are at $(7.8, 23.4, 39.0, 54.6, \dots) \times 10^{19}$ cm$^{-2}$. The slice for the position-velocity diagram was made along the dynamical major axis $\Gamma = 292°$. The $x$-axis indicates arcminutes northwest of the dynamical center. Contours and gray scales for the H I observed velocity field are from 1320 (east; *light shading*) to 1420 km s$^{-1}$ (west; *dark shading*) in increments of 10 km s$^{-1}$. The 1330, 1370, and 1410 km s$^{-1}$ contours are identified.

disk through an intergalactic medium. Interestingly, this would indicate that NGC 1042 is traveling in the direction opposite to the position of NGC 1052. Van Gorkom et al. (1986) also comment that the H I in NGC 1042 is not significantly larger in extent than the optical galaxy. Our estimate of $D_{\rm H\,I}/D_{25} = 1.7$, however, indicates a large H I disk and is close to the average for our sample.

The dynamics of NGC 1042 include substantial evidence along the minor axis of a warp in the disk, especially north

of the optical disk. Several other nonaxisymmetric kinematic features are indicated as well. One of these is the closed velocity contours on the eastern side of the galaxy, seen in both the velocity field and the channel maps, implying a peak in $V_{\rm rot}$ just inside the optical radius. This feature is also consistent with a warp. The warped disk is also manifest in the H I position angle curve, in which $\Gamma$ changes by as much as 43° as a function of radius. Streaming motions are apparent on both sides of the minor axis, corre-
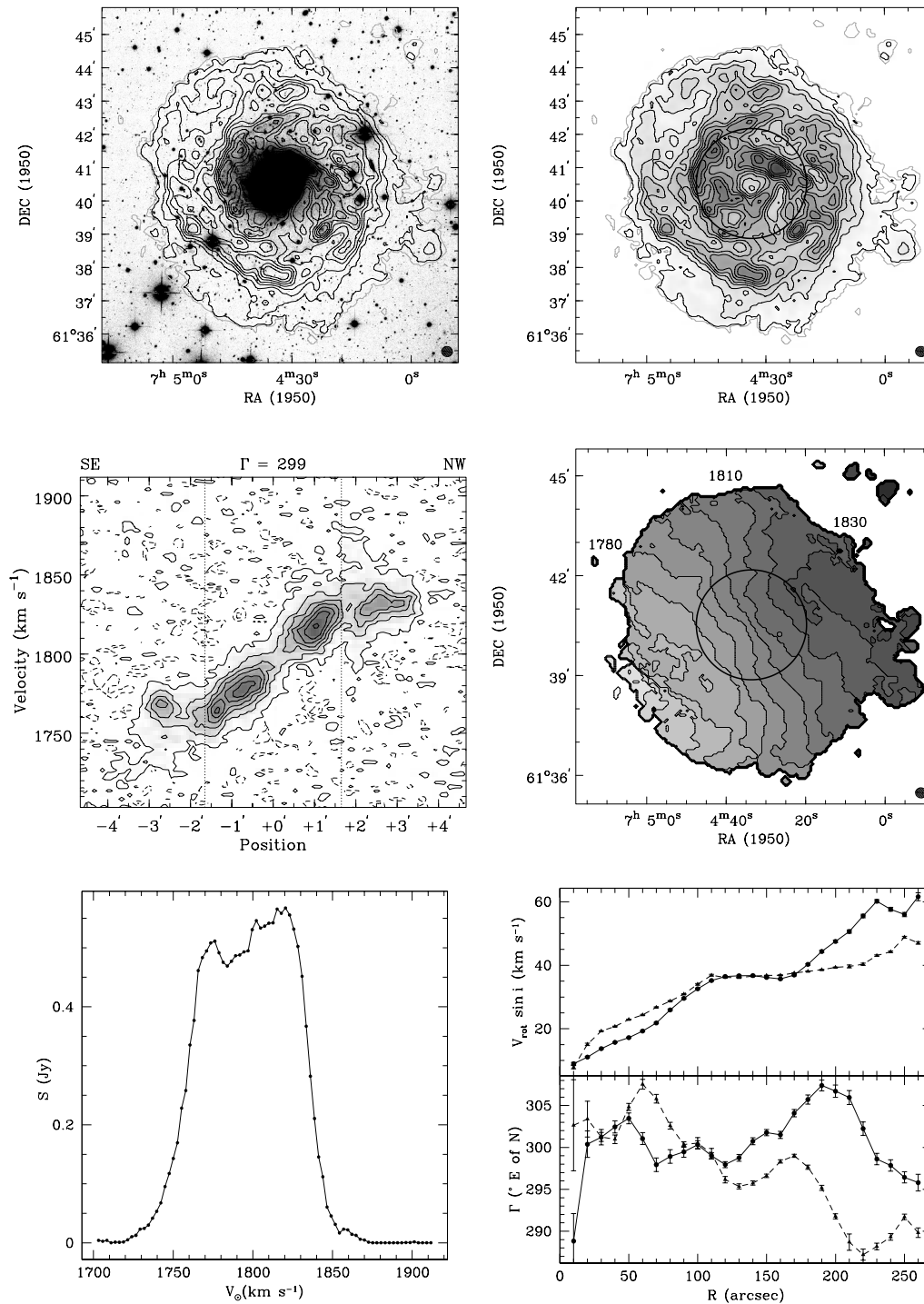
FIG. 4.—Same as Fig. 2, but for UGC 3685. Light gray H I column density contours are at $1.1 \times 10^{19}$ cm$^{-2}$ and solid contours at $(3.3, 13.2, 23.1, 33.0, \ldots)$ $\times 10^{19}$ cm$^{-2}$. The slice for the position-velocity diagram was made along the dynamical major axis $\Gamma = 299°$. The x-axis indicates arcminutes northwest of the dynamical center. Contours and gray scales for the H I observed velocity field are from 1730 (east; *light shading*) to 1830 km s$^{-1}$ (west; *dark shading*) in increments of 10 km s$^{-1}$. The 1780, 1810, and 1830 km s$^{-1}$ contours are identified.

lating with the outer extensions of the two dominant optical spiral arms. In NGC 1042 $V_{rot} \sin i(r)$ is reminiscent of rotation curves presented by S3vA, in which opposite sides rise with different slopes. These dynamical perturbations suggest tidal interaction with NGC 1052.

An interesting feature to note is that the position angle of the optical galaxy reported by KHL, found by fitting elliptical isophotes, appears perpendicular to the major axis of

the velocity field of the H I. This effect is apparent in Figure 3, where the morphological major axis of the low surface brightness optical galaxy appears to run north-south, while the dynamical major axis in the H I velocity field is clearly east-west. The implication is that the optical disk possesses inherent ellipticity, again suggesting tidal interaction with NGC 1052. Since KHL estimated inclinations based on optical axial ratios and the assumption of circular disks, the
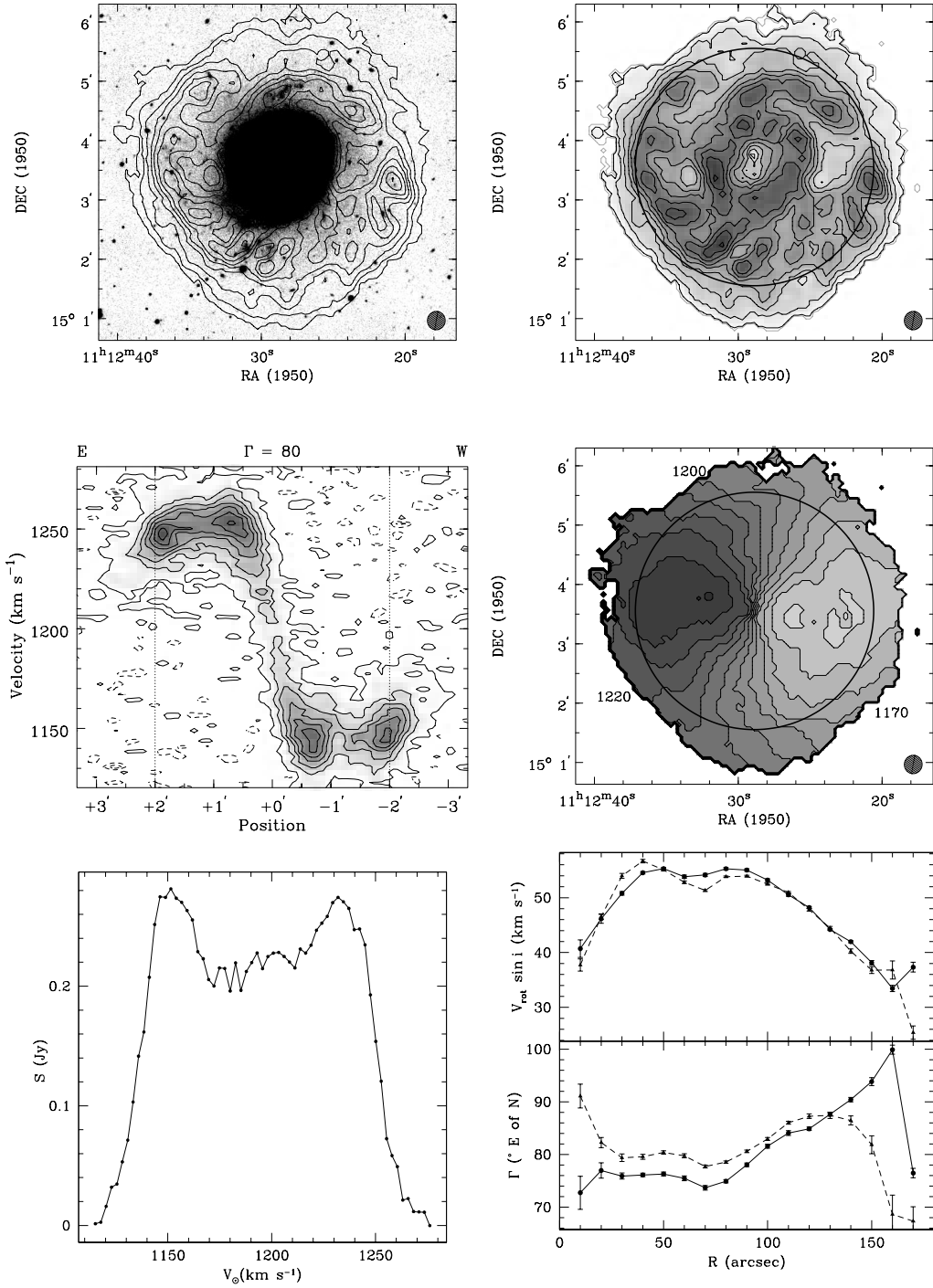
FIG. 5.—Same as Fig. 2, but for NGC 3596. H I column density contours are at $(0.05, 16.2, 28.35, 40.5, \ldots) \times 10^{19}$ cm$^{-2}$. The first contour represents the 3 $\sigma$ noise level. The slice for the position-velocity diagram was made along the dynamical major axis $\Gamma = 80°$. The $x$-axis indicates arcminutes west of the dynamical center. Contours and gray scales for the H I observed velocity field are from 1130 (west; *light shading*) to 1260 km s$^{-1}$ (east; *dark shading*) in increments of 10 km s$^{-1}$. The 1170, 1200, and 1220 km s$^{-1}$ contours are identified.

optical asymmetry parameter derived there is likely to be an underestimate. In this work, we use the dynamical position angle.

### 2.3.3. UGC 3685

UGC 3685 (Fig. 4) is a flocculent SBb galaxy whose bar terminates at a well-defined circular ring. Two major spiral arms extend outward from the ring, but their positions are uncorrelated with the bar. The northern spiral arm and

associated flocculent structure is more luminous than the southern structure and contains many bright H II regions. An additional area of low surface brightness extends to the northeast. It is classified as symmetric by KHL. There are no galaxies within 1° and 1000 km s$^{-1}$ of UGC 3685 listed in the AGC.

The neutral hydrogen distribution extends to a radius of $2.1R_{25}$. Not all of the single-dish flux was recovered during these observations, and although comparison with an H I
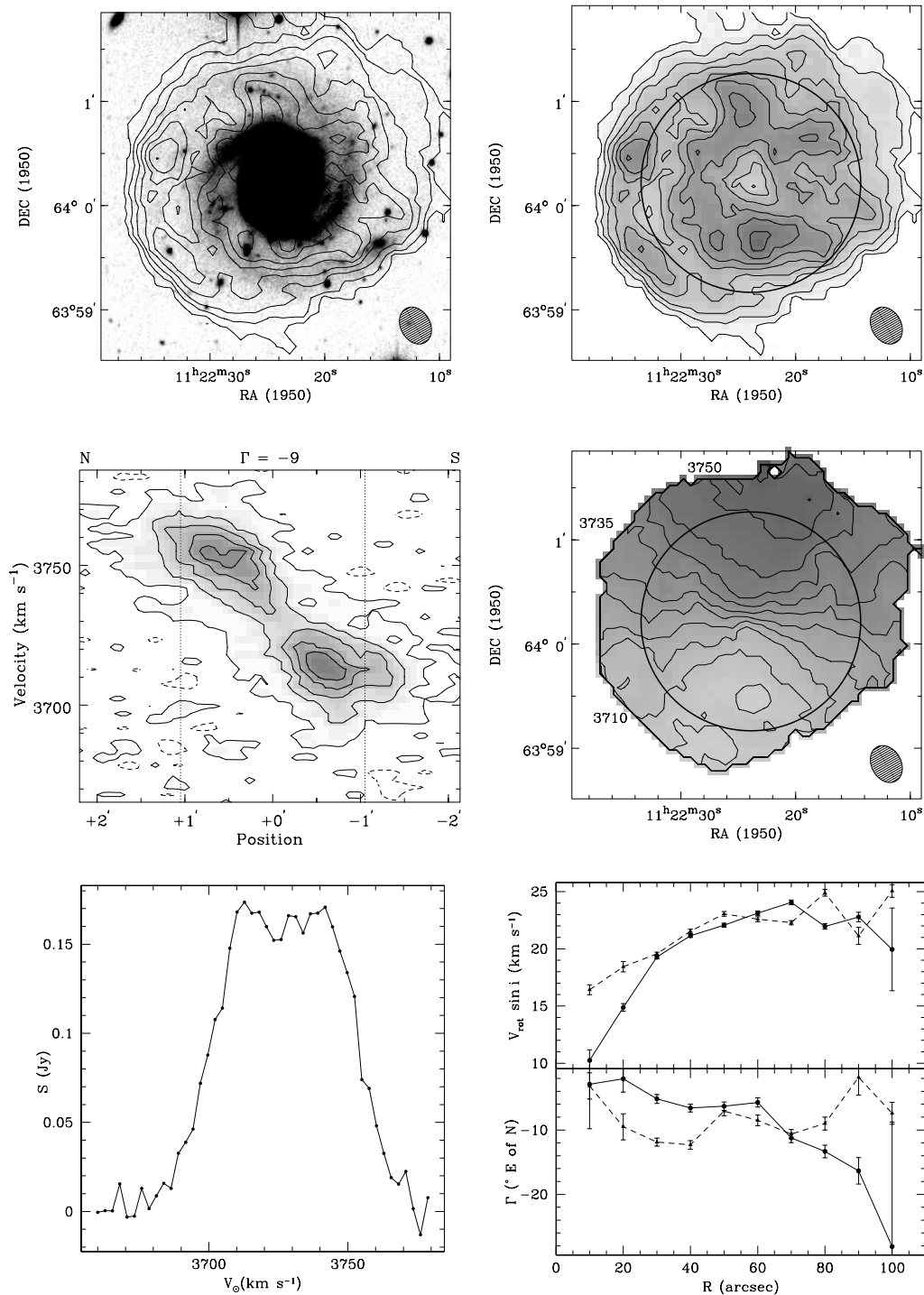
FIG. 6.—Same as Fig. 2, but for UGC 6429. H I column density contours are at $(5.4, 16.2, 27, 37.8, \ldots) \times 10^{19}$ cm$^{-2}$. The first contour represents the 3 $\sigma$ noise level. The slice for the position-velocity diagram was made along the dynamical major axis $\Gamma = -9°$. The x-axis indicates arcminutes north of the dynamical center. Contours and gray scales for the H I observed velocity field are from 3700 (south; *light shading*) to 3770 km s$^{-1}$ (north; *dark shading*) in increments of 5 km s$^{-1}$. The 3710, 3735, and 3750 km s$^{-1}$ contours are identified.

line profile obtained with the former 91 m telescope at Green Bank available in the digital archive of H I spectra of Giovanelli & Haynes indicates that much of the difference can be explained by calibration errors, additional low surface density diffuse gas whose flux was not detected at the VLA cannot be ruled out. The "fishtail," a small western extension of the distribution, occurs at the $10^{20}$ cm$^{-2}$ level, and, along with the H I gap to the northwest and strong

spiral structure, significantly affects the outcome of the morphological analysis. The overall dynamics of the neutral hydrogen seem relatively undisturbed, although streaming motions of 3–5 km s$^{-1}$ are apparent just outside the optical radius to the north and at $1.5R_{25}$ to the south, following the spiral arms. The rotation curve and line profile of the galaxy, however, are asymmetric between approaching and receding sides.
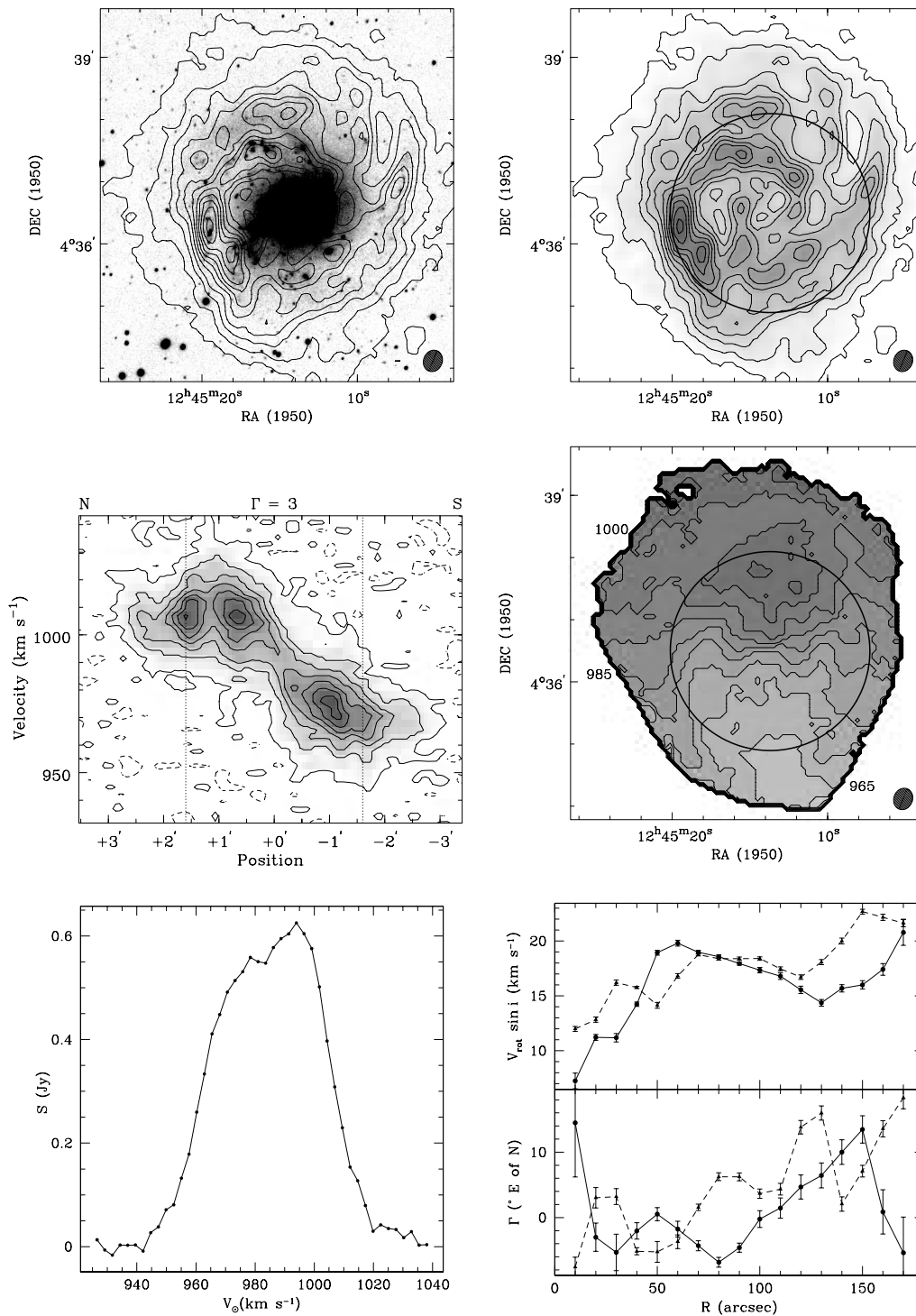
FIG. 7.—Same as Fig. 2, but for NGC 4688. H I column density contours are at $(7.2, 21.6, 36.0, 50.4, \ldots) \times 10^{19}$ cm$^{-2}$. The first contour represents the 3 $\sigma$ noise level. The slice for the position-velocity diagram was made along the dynamical major axis $\Gamma = 3°$. The x-axis indicates arcminutes north of the dynamical center. Contours and gray scales for the H I observed velocity field are from 960 (south; *light shading*) to 1010 km s$^{-1}$ (north; *dark shading*) in increments of 5 km s$^{-1}$. The 960, 980, and 1000 km s$^{-1}$ contours are identified. The synthesized H I line profile was obtained by integrating the data cube along both spatial axes in the region containing flux from NGC 4688. The profile does not include flux from the companion.

The most interesting dynamical feature of UGC 3685 appears in the position-velocity diagram and the channel maps. A region of high (40 km s$^{-1}$) velocity dispersion is detected 2′ northwest of the galactic nucleus at an azimuth of approximately 299°. This feature is consistent with the presence of a superbubble, an outflow of hot gas into the halo as a result of rapid star formation and Type II super-

novae in large H II regions. The symmetry in the velocity contours above and below the systematic rotational velocity of the remainder of the disk implies that the bubble originated with an event near the midplane of the disk. A similar H I bubble has been observed in M101 by Kamphuis, Sancisi, & van der Hulst (1991). The bubble in UGC 3685 is observed nearly normal to the disk, allowing the
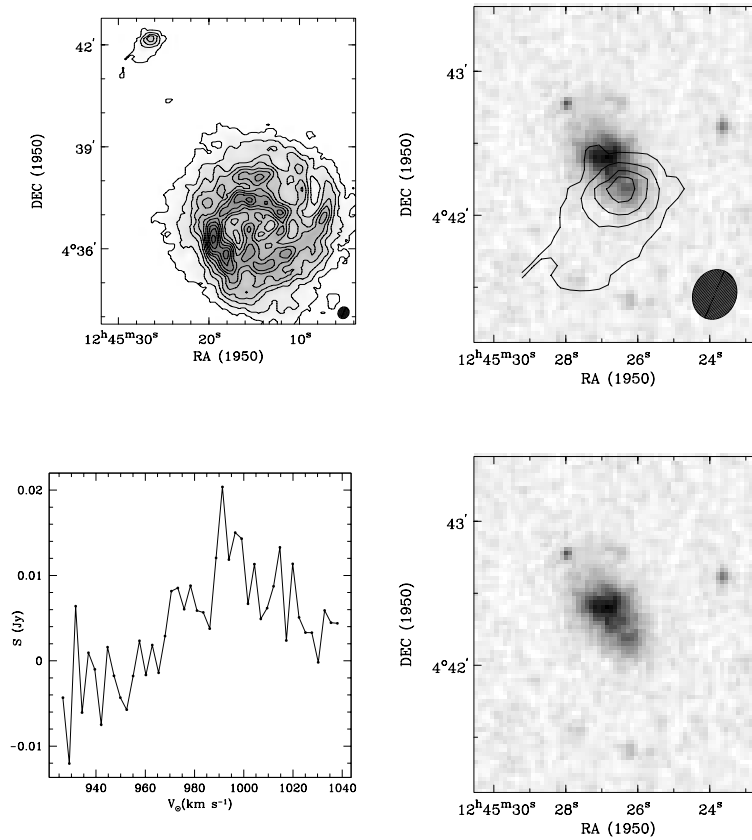
Fig. 8.—Wide-field VLA H I synthesis data for CGCG 043-029, the companion of NGC 4688. *Top left*: of NGC 4688 and companion. The contours and gray scales are as in Fig. 7. *Top right*: H I column density of the companion object alone, overlaid on the POSS image of the region. *Bottom left*: Integrated line profile of the companion alone, obtained by integrating both spatial axes of the data cube in the region containing flux from the companion. *Bottom right*: POSS image of CGCG 043-029 without the H I contours, showing clearly the two distinct optical maxima.

enclosed kinetic energy of expansion into the halo to be directly measured. The H I mass enclosed in the bubble is $1.22 \times 10^7 \, M_\odot$, resulting in an approximate kinetic energy of $2 \times 10^{53}$ ergs, of the same order as energies found in superbubbles in M101.

### 2.3.4. NGC 3596

NGC 3596 (Fig. 5) is an optically asymmetric Sc galaxy which exhibits two " grand design " spiral arms surrounded by a low surface brightness system of flocculent structure. The contrast of the optical image in the accompanying figure was selected to emphasize the flocculent outer structure so that the relationship between this structure and the H I morphology is clearer. The neutral gas in NGC 3596 is distributed in a ring comparable in radius to the bright spiral arms, from which extends high column density spiral structure in the south, while a single H I spiral arm extends to the north. The northern arm and the highest column density southern arm correspond to very low surface brightness features in the optical; however, the optical features do not extend coherently along the entire length of the gas features. While the northern H I arm overlies its corresponding flocculent optical arm, the optical feature associated with the greatest H I column density in the southern arm is offset from the H I by 10″ (0.7 kpc) to the east. The remaining H I spiral arms overlie corresponding low surface brightness flocculent structures. The overall asymmetric distribution of neutral gas contributes to a relatively high value of the morphological asymmetry parameters for this target.

Although there are no galaxies within 1° of NGC 3596 with known redshifts near 1193 km s$^{-1}$ listed in the AGC, NGC 3596 is dynamically perturbed. Although the H I disk does not extend far beyond the optical radius and the inner velocity contours of the galaxy appear very regular, warping is evident beyond $R_{25}$, and the dynamical position angle of the approaching side varies southward by as much as 31°. The severity of the warp is most evident in the channel maps, in which the disk appears so warped that several channels on both the approaching and receding sides contain flux in a circular or multiple-component pattern. Closed contours are evident on both the receding and approaching sides, and the galaxy exhibits a falling $V_{\rm rot} \sin i(r)$, indicating a warp. The line profile of the galaxy, however, is quite symmetric, hiding the inherent dynamic nonaxisymmetry, in agreement with HHMRvZ.

### 2.3.5. UGC 6429

As measured by KHL, UGC 6429 (Fig. 6) is optically an asymmetric Sc disk exhibiting two inner and two outer spiral arms, with the southern arm terminating in a large, bright H II region. The H I distribution exhibits an asymmetric ring following the inner spiral arms, and a large high column density feature to the east, just outside $R_{25}$. This feature is an extension of the northern optical outer spiral arm, which gives the entire distribution a very asymmetric qualitative appearance.

Dynamically, the most apparent departures from axisymmetry in UGC 6429 are the closed contours on the approaching side of the velocity field and the change in
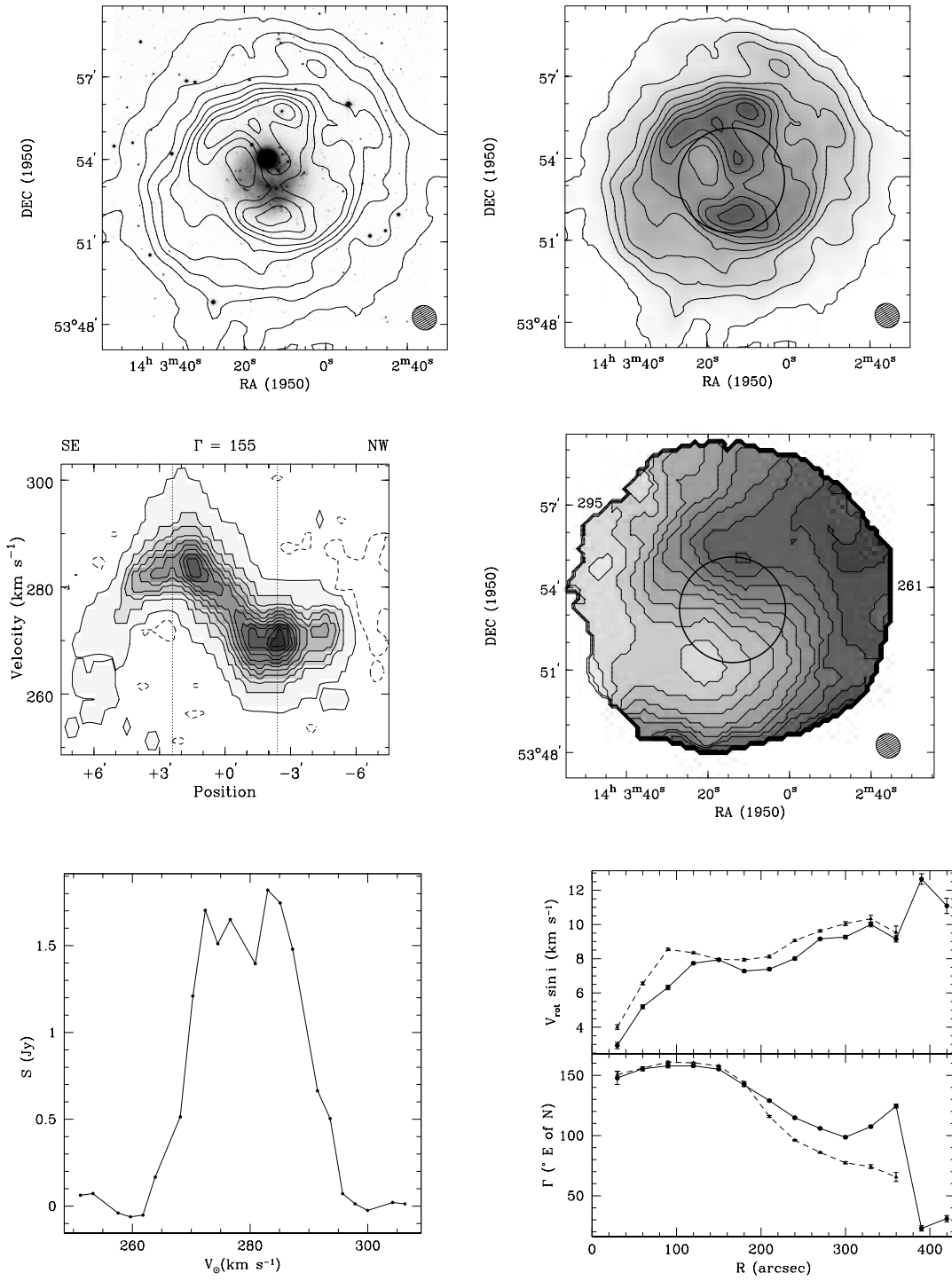
FIG. 9.—Same as Fig. 2, but for NGC 5474 from archive data originally obtained by RDH. H I column density contours are at $(1.8, 10.8, 19.8, 28.8, \ldots)$ $\times 10^{19}$ cm$^{-2}$. The first contour represents the 3 $\sigma$ noise level. The slice for the position-velocity diagram was made along the dynamical major axis $\Gamma = 155°$. The $x$-axis indicates arcminutes southeast of the dynamical center. Contours and gray scales for the H I observed velocity field are from 259 (west; *light shading*) to 297 km s$^{-1}$ (*dark shading*) in increments of 4 km s$^{-1}$. The 295 and 261 km s$^{-1}$ contours are identified.

position angle with radius to the north. There is no dynamical feature corresponding to the eastern morphological feature. The asymmetry in the integrated line profile of this galaxy is due to the nonuniform weights given in integrating

the line profile because of the eastern density enhancement. The nearest neighbor to UGC 6429 listed in the AGC is NGC 3668, 17′ (371 kpc in projected distance) to the southeast, at 3508 km s$^{-1}$.
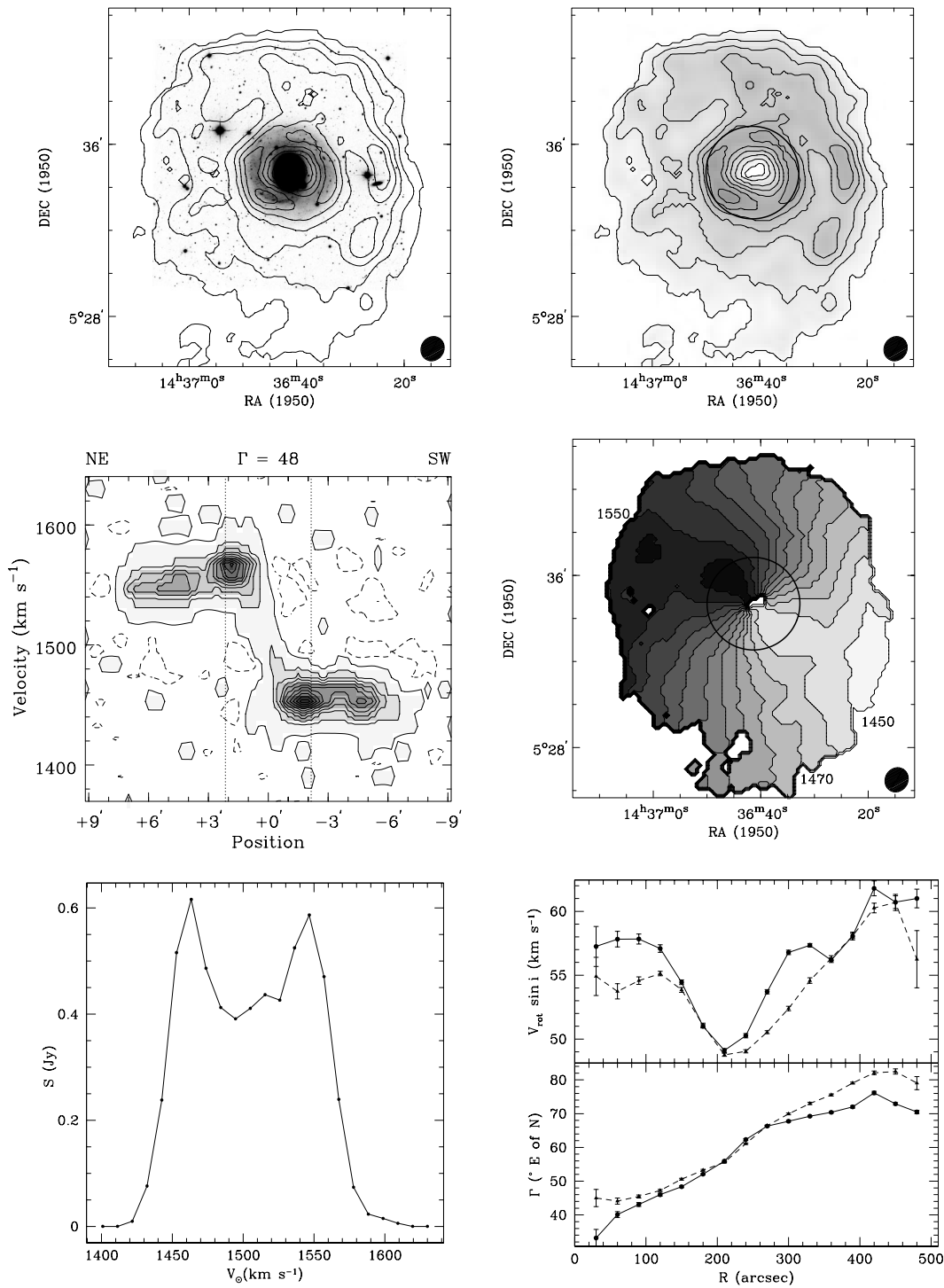
FIG. 10.—Same as Fig. 2, but for NGC 5701 from VLA archive data originally observed by S. E. Schneider. H I column density contours are at (2.9, 7.8, 12.7, 17.6, ...) × $10^{19}$ cm$^{-2}$. The slice for the position-velocity diagram was made along the dynamical major axis $\Gamma = 48°$. The x-axis indicates arcminutes northeast of the dynamical center. Contours and gray scales for the H I observed velocity field are from 1440 (west; *light shading*) to 1560 km s$^{-1}$ (east; *dark shading*) in increments of 10 km s$^{-1}$. The 1450, 1470, and 1550 km s$^{-1}$ contours are identified.

### 2.3.6. *NGC 4688*

NGC 4688 (Fig. 7) is an outlying member of the Virgo Cluster, and is a member of LGG 292 (Garcia 1993). Its nearest neighbor listed in that group is UGC 7983, an irregular galaxy 43' (213 kpc at the adopted distance of 17 Mpc) to the southeast. NGC 4688 is a very asymmetric Scd galaxy in the optical, where flocculent spiral arms extend away from the main body of the galaxy to the northeast. Except for the tidally deformed galaxy NGC 5474, NGC 4688 is the most optically asymmetric galaxy in the sample. The H I morphology, too, exhibits strong asymmetries, particularly the very high column density regions to the east-southeast just at $R_{25}$. These regions correspond to the southernmost of the flocculent optical arms as seen in the R
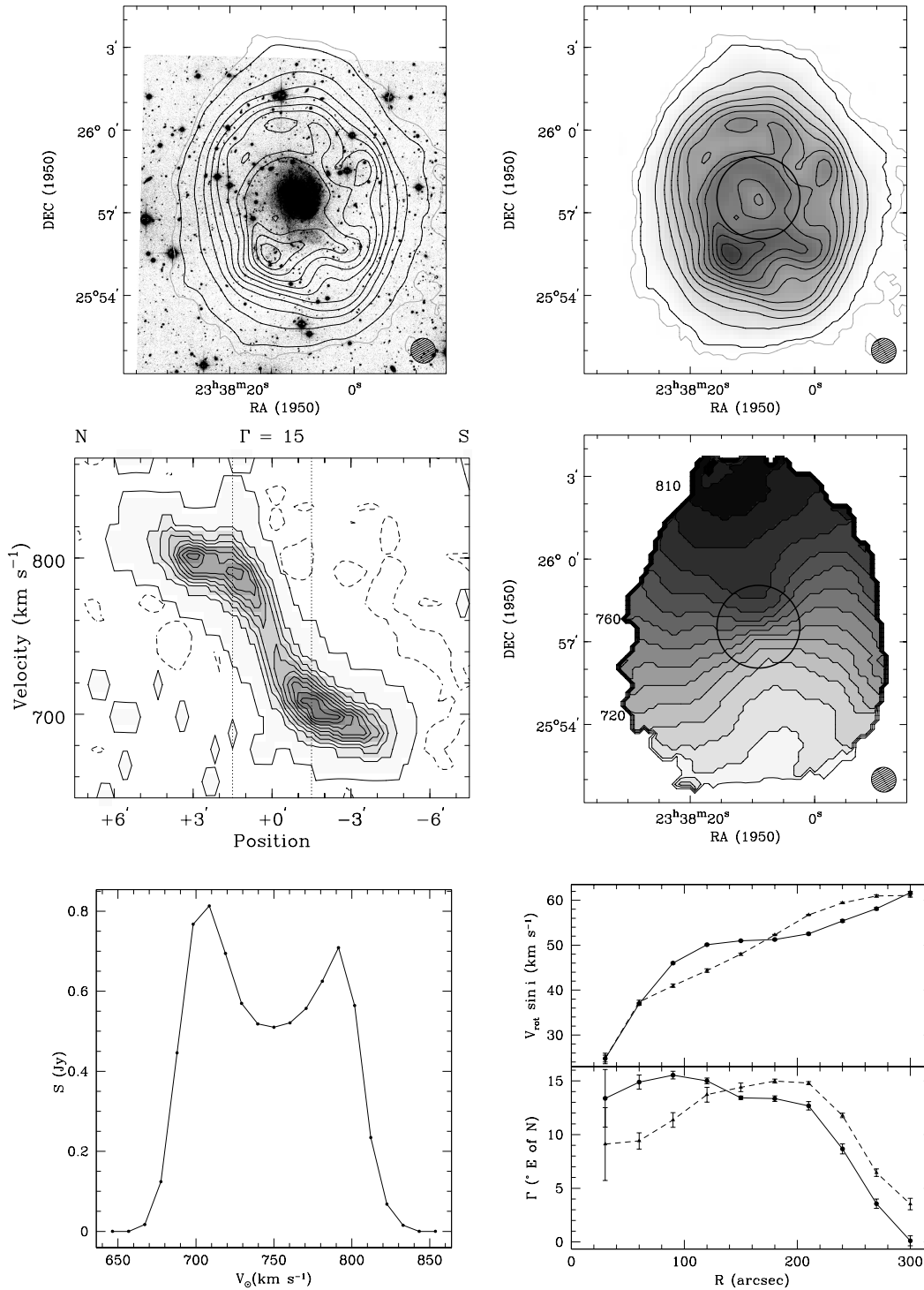
Fig. 11.—Same as Fig. 2, but for UGC 12732 from VLA archive data originally observed by Schulman et al. (1997). Light gray contours are at $6.7 \times 10^{18}$ cm$^{-2}$ and solid contours at $(2.0, 11.4, 20.8, 30.2, \ldots) \times 10^{19}$ cm$^{-2}$. The first solid contour represents the 3 $\sigma$ noise level. The slice for the position-velocity diagram was made along the dynamical position angle $\Gamma = 15°$. The $x$-axis represents arcminutes north of the dynamical center. Contours and gray scales for the H I observed velocity field are from 680 (south; *light shading*) to 810 km s$^{-1}$ (east; *dark shading*) in increments of 5 km s$^{-1}$. The 720, 760, and 810 km s$^{-1}$ contours are identified.

band. Spiral structure, in fact, can be seen throughout the H I disk, corresponding to flocculent structures in the optical galaxy. The low column density H I is distributed preferentially to the northeast, lending an even more qualitative lopsided appearance to the galaxy. This feature contributes to a larger value of $R_{\rm H I}/R_{25}$ to the north than to the south. Quantitatively, as calculated in the next section, the morphological asymmetry of the H I distribution makes

NGC 4688 the most morphologically asymmetric galaxy in gas as well as in optical light.

Dynamically, too, NGC 4688 is disturbed. The receding side of the velocity field exhibits closed contours that reopen again at $1.5R_{25}$, a feature similar to that found in NGC 991 and NGC 5474. This feature leads to a large asymmetry in the rotation curve, which manifests itself as a large difference between observed velocity on the approach-

ing and receding sides at the same radius. The global profile is unusual too, in that it exhibits very gradual declines from the peaks to the noise level on both sides of the profile.

A possible explanation for this very asymmetric behavior lies $6.\!^{\prime}7$ (33 kpc) to the northeast of the dynamical center of NGC 4688: a small $3.2 \times 10^7 \ M_\odot$ companion detected in the H I map. The peak of the H I distribution of the companion is located at B1950.0 coordinates $(\alpha, \ \delta) =$ $(12^h45^m26.\!^s5, \ +04°42'10'')$. The systemic velocity of the peak of the companion's emission is 991 km s$^{-1}$.

The column density map of the companion is presented in Figure 8. The top left panel of this figure presents the column density of NGC 4688 and the companion for scaling; the top and bottom right panels detail the companion itself. The H I column density contours in the top right panel are overlaid on the Palomar Observatory Sky Survey[8] plate for this region digitized by the Space Telescope Science Institute Digitized Sky Surveys[9]. The bottom

right panel depicts the POSS plate alone. The companion is just resolved by our observations in the CS configuration, and the maximum column density observed is $6 \times 10^{20}$ cm$^{-2}$. An optical counterpart to the H I emission is clearly seen. The observed location of the H I emission, however, is offset 20$''$ to the southwest of the maximum of the optical emission, but it does correspond to a smaller local maximum. We identify these two optical maxima as the galaxy pair CGCG 043-029. The bottom left panel of Figure 8 illustrates the synthesized line profile of this object. The maximum flux occurs in the 991 km s$^{-1}$ channel. The gradual slope on the receding side of the profile, however, suggests that there is probably significant additional flux beyond our velocity limit of 1040 km s$^{-1}$.

An H I detection from the northeastern component of CGCG 043-029 appears in a table of H I observations of faint galaxies conducted with the Arecibo circular feed compiled by Lu et al. (1993), except that the heliocentric velocity reported there is 4889 km s$^{-1}$. It is a possibility, therefore, that the pair is an optical pair only, with the 4889 km s$^{-1}$ emission associated with the northeastern component, and the 991 km s$^{-1}$ emission associated with the southwestern component. The data, however, are too incomplete for us to make any supportable claims regarding this object beyond its mere detection.

During the initial analysis of the 21 cm line data, we imaged the data cube using a tapered beam of size $40'' \times 45''$ to examine the data for evidence of an H I bridge
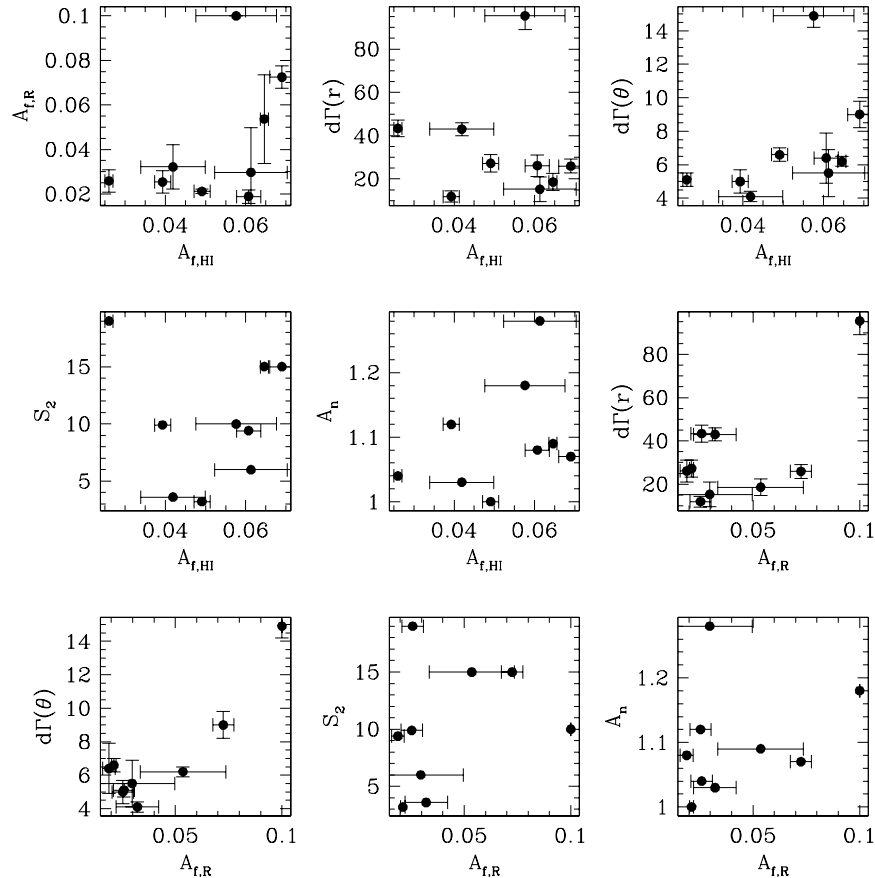
---

[8] The National Geographic Society–Palomar Observatory Sky Atlas (POSS I) was made by the California Institute of Technology with grants from the National Geographic Society.

[9] The Digitized Sky Surveys were produced at the Space Telescope Science Institute under US grant NAGW-2166. The images of these surveys are based on photographic data obtained using the Oschin Schmidt Telescope on Palomar Mountain and the UK Schmidt Telescope. The plates were processed into the present compressed digital form with the permission of these institutions.



Fig. 12.—Observed relationships between the morphological asymmetry parameters, $A_{f,\mathrm{H\,I}}$ and $A_{f,R}$, and the dynamical parameters measuring position angle change with radius, $\Delta\Gamma(r)$; position angle change from approaching to receding side, $\Delta\Gamma(\theta)$, $3V_{\mathrm{rot}} \sin i (r)$; curve asymmetry, $S_2$; and integrated H I line profile asymmetry, $A_n$.

between NGC 4688 and CGCG 043-029. No such bridge was detected.

### 2.3.7. *NGC 5474*

NGC 5474 (Fig. 9) is a peculiar spiral galaxy approximately 44′ (90 kpc at the adopted distance of 7 Mpc) to the south of M101 and is tidally deformed into a very asymmetric and disturbed morphology, as observed by KHL in the optical. NGC 5474 was first observed in H I synthesis by van der Hulst & Huchtmeier (1979) at the Westerbork synthesis radio telescope, with significant H I flux appearing in four channels with a velocity resolution of 27.2 km s$^{-1}$. Subsequently, this galaxy was observed by RDH with the D configuration at the VLA. Both groups indicate that the kinematic major axis of this galaxy does not appear to form a straight line, but rather is contorted into an S shape. They also note that the kinematic center and morphological centroid of the H I distribution are approximately colocated with the center of the outer optical isophotes and not with the offset optical nucleus. Hence, the true center of the galaxy is not the bright "pseudonuclear" region located to the north of the overall optical light distribution.

We are able to trace H I to a radius of approximately 400″, in contrast to the 250″ radius recovered by RDH and by van der Hulst & Huchtmeier. In addition to the "clumps" of neutral hydrogen found in the high H I column density regions by RDH, we find a smooth H I distribution beyond twice the optical radius. Even so, only half the reported single-dish flux for this galaxy was recovered, because NGC 5474 and M101 share a common H I distribution (Huchtmeier & Witzel 1979), and even the short spacings of the D configuration are unable to recover the diffuse gas that envelops this galaxy and its dominant com-

panion. We do, however, detect 50% more flux than that found by RDH.

Dynamically, the galaxy exhibits a number of bizarre features. RDH detect 50° of position angle change from the dynamical center to a radius of 250″. Our reanalysis agrees with their analysis and also reveals the continuation of this trend farther out, where the position angle varies by a total of 95° from the dynamical center to a 400″ radius. Position angles for the approaching and receding sides also diverge in the outer regions; the difference in position angle from one side to the other is ≈50°, although the greatest divergence occurs in a region of small signal-to-noise ratio (slightly below 3 $\sigma$) and may therefore be an artifact of the model. These large position angle variations as a function of radius are largely due to the very unusual dynamic feature found 40″ to the south of the optical center of the galaxy disk, in which the velocity contours fully reverse their directions, a continuation of the S shape reported by the previous observers. This feature also displaces the dynamical center of the outer regions about 1′ to the southwest of the optical pseudonucleus center of light. The feature contributes to the measurable asymmetry in the integrated single-dish line profile. Such a feature may be the result a very warped disk viewed in a direction that bisects the angle formed by the flat and warped portions of the disk. The pseudonucleus itself has no discernible effect on the dynamics of the disk.

RDH use a model in which the galaxy inclination is fixed at 21° to determine their rotation curve; if we fix the inclination at this value, we recover the same curve. Both analyses agree on the general shape of the curve, which rises out to about 100″, is steeper on the receding side, and flattens out with a shallow minimum at 200″.

### 2.3.8. *NGC 5701*

The barred Sa galaxy NGC 5701 (Fig. 10) exhibits prominent inner and outer ring structures in the optical image along with a large bulge and bar at position angle −5°. The optical galaxy is embedded in a very large H I envelope of $D_{\rm H I}/D_{25} = 2.6$. More H I flux is observed on the west side of the galaxy than on the east by a factor of 2, and the western drop-off is more precipitous than the east. This feature is similar to that found in NGC 1042 (§ 2.3.2), where it is interpreted as a possible remnant of tidal interaction. In this case, however, no companion to NGC 5701 is seen in our optical or H I data. It is, however, identified by Garcia (1993) as a member of the group LGG 386, of which the nearest member to NGC 5701 is UGC 9385, which is 57′ (431 kpc at the adopted distance of 26 Mpc) to the west.

In this connection, it is important to note that NGC 5701 was also mapped at Arecibo by DuPrie & Schneider (1996). We agree with their Figure 3, that the H I is extended to ∼10′; however, we do not recover the H I "cloud" they report 15′ northwest of the center of NGC 5701 with flux 5.5 Jy km s$^{-1}$. We do detect two flux peaks 4 $\sigma$ above the noise 13′ to the northwest in two channels (1495 and 1505 km s$^{-1}$) in the archive data. However, because the emission peaks occur in two different spatial locations separated by about a beam width, these peaks were excluded from the moment maps by the windowing function. That these peaks occur at the same heliocentric velocity as the cloud reported by DuPrie & Schneider and would represent a total flux of 4.6 Jy km s$^{-1}$ suggests that the cloud is marginally detected in the synthesis data.
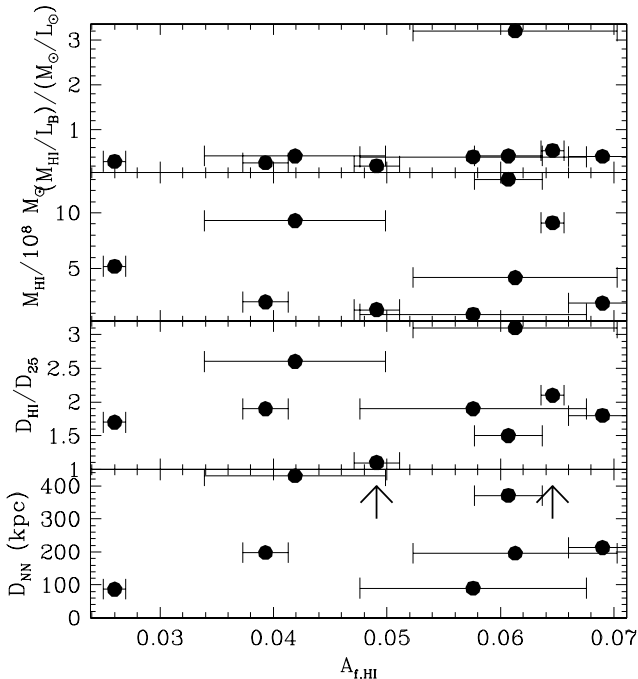


FIG. 13.—Relationships between H I morphology and the global H I parameters. *Top to bottom*: mass-to-light ratio in solar units; H I mass; H I diameter in terms of optical diameter, $D_{25}$; and projected distance to the nearest neighbor. The positions of UGC 3685 and NGC 3596, which have no neighbors within 1°, are indicated by arrows.
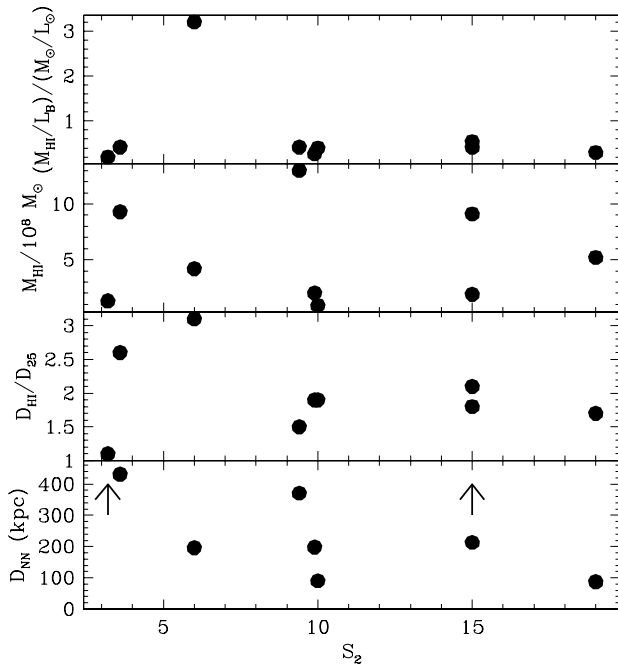
Fig. 14.—Relationships between rotation curve asymmetry, $S_2$, and the global H I parameters examined in Fig. 13.

Nonlinearity of the velocity contours along the minor axis of NGC 5701 can be observed in the velocity field. This results in a dynamical position angle change of 43° as a function of radius, similar to the value obtained from analysis of NGC 1042. NGC 5701 also exhibits significant differences between the values of $V_{rot} \sin i(r)$ on either branch of the major axis, again similar to the rotation curve of NGC 1042. NGC 5701 differs, however, in that it exhibits a deep trough in $V_{rot} \sin i(r)$ at a radius of 210″. This suggests either a warp or strong streaming motions in this galaxy. The synthesized line profile of NGC 5701 is consistent with the single-dish profile presented by HHMRvZ. In agreement with them, we find that the profile is symmetric.

### 2.3.9. UGC 12732

UGC 12732 (Fig. 11), first observed by Schulman et al. (1997), is a small Sm galaxy with a roughly symmetric optical appearance. Compared with the optical galaxy, the neutral gas structure detected is extremely large: $D_{H I}/D_{25} = 3.1$ as listed in Table 3 and $M_{H I}/L_B$ is an order of magnitude greater than that of the other targets. Indeed, UGC 12732 is more gas-rich (or star-poor) than most Sm galaxies; $M_H/L_B$ of 3.2 is well in excess of the median of 0.78 for Sm and Im galaxies given by Roberts & Haynes (1994). The nearest neighbor of known redshift within 1000 km s⁻¹ to that of UGC 12732 is NGC 7741, 45′ (196 kpc) to the southeast, at 744 km s⁻¹.

The contours in Figure 11 were chosen to emphasize the spiral structure slightly to the north of the optical galaxy. This spiral structure does not appear to be associated with any optical spiral structure. The region of maximum H I column density is located approximately 2′ to the south-southeast of the optical center, which corresponds to the termination of the eastern spiral arm as seen in the R band. The outer H I density contours are centered on the optical center of light, as is a 1′ radius ring surrounding the inner

regions of the optical galaxy. The spiral structures extend from this ring and are especially apparent to the northwest. These structures contribute to a very high value of morphological asymmetry for the neutral hydrogen distribution. In dynamics, a 30° position angle change on both the approaching and receding sides of the galaxy, rising $V_{rot} \sin i(r)$, and an asymmetric line profile contribute to overall dynamical nonaxisymmetry in UGC 12732.

As Schulman et al. commented, the large $D_{H I}/D_{25}$ ratio may be an indicator of inefficient star formation in this galaxy. The $V_{rot} \sin i(r)$ curve and position angle fits we derive with the tilted-ring model differ from those derived by Schulman et al. in that the qualitative shapes of the curves differ significantly between the two analyses. While in the Schulman et al. analysis, the inclination was allowed to vary to obtain a flatter rotation curve, our analysis does not attempt to disentangle $i$ from $V_{rot}$, resulting in a rising $V_{rot} \sin i(r)$ curve and a greater change in position angle as a function of radius.

## 3. COMPARING MORPHOLOGICAL AND KINEMATIC ASYMMETRY

### 3.1. Obtaining the Various Measures of Asymmetry in a Galaxy

We examined our data sets for any correlations between asymmetric morphology and nonaxisymmetric dynamics. In doing so, we wished to search for methods of quantifying deviations from kinematic axisymmetry, including both nonplanar and noncircular motions, which could then be compared with the morphological measures. Dynamic models of the galaxies allowed us to define several kinematic quantities that, we hypothesized, might be correlated with asymmetric morphology. The features we examined were morphological asymmetry in $R$ band and H I, change of kinematic position angle with radius, change of kinematic position angle with azimuth, and asymmetry in rotation curves. Single-dish H I line profile asymmetry was also computed for these galaxies, using the method described by HHMRvZ.

The zeroth-order H I moment maps were analyzed for morphological asymmetry, using the method of sectors described in KHL. Each galaxy was divided into eight equal-area sectors with the center of the pattern located at the optical center of light and the position angle of the sector pattern oriented along the dynamical position angle of the galaxy. The total H I flux was measured in each of the sectors. The maximum flux differences were then normalized by the total integrated H I flux through the pattern. The result is the asymmetry parameter,

$$A_f \equiv \Delta f^{max} \bigg/ \sum_n f_n , \qquad (7)$$

where $\Delta f^{max}$ is the largest flux difference between any two sectors and $f_n$ is the flux in the $n$th sector.

$R$-band values of $A_{f,R}$ are presented here, adapted from the data used by KHL. KHL presented sector analysis of optical data by taking the ratio of the maximum flux in a sector to the minimum flux in a sector and converting this to a magnitude difference in the standard way. Thus, KHL present the data in terms of magnitude differences $\Delta M$ between sectors rather than normalized flux differences. In their work, a galaxy was said to be asymmetric if a value of $\Delta M$ differed from zero by more than the 5 σ rms noise level,

regardless of the magnitude of $\Delta M$ itself. For this reason, some galaxies with large values of $\Delta M$ were classified as symmetric because the errors were also large. Similarly, small values of $\Delta M$ with small errors could indicate asymmetric galaxies. Of the nine galaxies considered here, UGC 3685, NGC 5701, and UGC 12732 were classified as symmetric; all others were classified as asymmetric. Here we use the same flux data as were used by KHL, but present them as normalized flux differences $A_f$ for both the optical and H I data because they are more useful in this form for understanding the symmetry properties of galaxy morphology in an absolute and directly comparable sense.

Deviations from axisymmetric dynamics of the targets were measured using data obtained from the model fitting. Because a symmetric flat rotating disk should exhibit a constant position angle, we took changes in position angle in the model as quantifiers of nonaxisymmetry. The first of these is the maximum change in position angle on one side of the galaxy as a function of radius, $\Delta\Gamma(r)$. Note that in cases in which the position angle changes steadily with radius, $\Delta\Gamma(r)$ can depend on the maximum radius for which we can construct a model. As applied to these face-on galaxies, $\Delta\Gamma(r)$ is most sensitive to nonplanar, as opposed to noncircular, motions. The second of these is the difference between position angles on approaching and receding sides of the model at the same radius averaged over all radii, $\Delta\Gamma(\theta)$. $\Delta\Gamma(\theta)$ is sensitive to noncircular motions and asymmetric warps.

Extending the analysis of S3vA, asymmetry in $V_{\rm rot} \sin i(r)$ curves was quantified in the following way. The curve was folded over the kinematic center of the model. The total area between the two curves was then measured and normalized by the average area under the curve to produce the measure of global rotation asymmetry,

$$S_2 \equiv 10^2 \frac{\int ||V_{\rm rot}(r) \sin i(r)| - |V_{\rm rot}(-r) \sin i(-r)|| \, dr}{\int \frac{1}{2}[|V_{\rm rot}(r) \sin i(r)| + |V_{\rm rot}(-r) \sin i(-r)|] \, dr} .$$

$$(8)$$

Clearly, for more inclined galaxies where $V_{\rm rot}$ and $i$ can be fitted separately, $S_2$ can be modified to measure asymmetry in $V_{\rm rot}(r)$ alone. In our sample of face-on galaxies, $S_2$ is very sensitive to nonplanar motions. In more inclined samples, $S_2$ would be more sensitive to noncircular motions.

Because several groups (e.g., Tifft & Cocke 1988; Richter & Sancisi 1994; HHMRvZ) have studied the symmetry

properties of 21 cm line profiles as an indicator of dynamical asymmetry in a galaxy, here too we apply the method of line profile asymmetry described by HHMRvZ. The quantity defined there is

$$A_{l/h} \equiv \frac{\int_{V_l}^{V_{\rm med}} S \, dV}{\int_{V_{\rm med}}^{V_h} S \, dV} ,$$

$$(9)$$

where $V_l$ and $V_h$ are the low and high velocity limits, respectively, of signal detection above 3 $\sigma$ and $V_{\rm med}$ is the median between them. The characteristic lopsidedness of the line profile is given simply by

$$A_n \equiv \begin{cases} A_{l/h}, & \text{if } A_{l/h} > 1 \\ 1/A_{l/h}, & \text{otherwise} . \end{cases}$$

$$(10)$$

The values of $A_n$ of 1.00 and 1.03 obtained in this work for NGC 3596 and NGC 5701, respectively, agree with the value $1/0.99 = 1.01$ obtained by HHMRvZ within errors and differences in velocity resolution. HHMRvZ found that approximately 50% of the line profiles studied exhibited asymmetry parameters $A_n \geq 1.05$, which they considered to be indicative of overall asymmetry.

Results for the asymmetry measures for each target are presented in Table 4. A plot of $A_{f,R}$ versus $A_{f,\rm HI}$ and the plots of all morphological-dynamical pairs are presented in Figure 12. This figure excludes points for NGC 5474, because of its large lower bound on $A_{f,R}$. Errors in $A_n$ are the size of the points, while systematic errors in $S_2$ we estimate at about 20%. Little correlation is apparent in our data set between H I morphology and dynamics for disk galaxies in the field. In our sample, there is a relationship between the H I and R-band morphologies in which large values of $A_{f,R}$ imply large values of $A_{f,\rm HI}$, although not the converse. It should not be surprising to find that optical and H I morphology are related, because H I spiral structure tends to follow the optical spiral structure.

All pairs of morphological versus dynamical parameters were also examined. The only statistically significant relationship between $A_f$ and any of the calculated dynamical parameters is a weak relation with $\Delta\Gamma(\theta)$. Large values of $\Delta\Gamma(\theta)$ imply large values of $A_{f,\rm HI}$ within our sample, but again, not the converse. It is also interesting that some of the most morphologically symmetric galaxies exhibit asymmetry in their line profiles as measured by $A_n > 1.05$. This qualitative observation and the lack of correlation between these parameters seems to support the casual observations of HHMRvZ and others who have noted a similar noncor-

TABLE 4

TARGET SYMMETRY PROPERTIES

| Galaxy (1) | $A_{f,R}$ (2) | $A_{f,\rm HI}$ (3) | $\Delta\Gamma(r)$ (deg) (4) | $\Delta\Gamma(\theta)$ (deg) (5) | $S_2$ (6) | $A_n$ (7) |
|---|---|---|---|---|---|---|
| NGC 991 ........ | $0.0254 \pm .005$ | $0.0393 \pm 0.002$ | $11.9 \pm 2.5$ | $5.0 \pm 0.7$ | 9.9 | 1.12 |
| NGC 1042 ....... | $0.0259 \pm .005$ | $0.0260 \pm 0.001$ | $43.4 \pm 3.9$ | $5.1 \pm 0.4$ | 19 | 1.04 |
| UGC 3685 ....... | $0.0536 \pm .02$ | $0.0646 \pm 0.001$ | $18.6 \pm 3.9$ | $6.2 \pm 0.3$ | 15 | 1.09 |
| NGC 3596 ....... | $0.0212 \pm .001$ | $0.0491 \pm 0.002$ | $27.2 \pm 4.0$ | $6.6 \pm 0.4$ | 3.2 | 1.00 |
| UGC 6429 ....... | $0.0189 \pm .003$ | $0.0607 \pm 0.003$ | $26.1 \pm 5.0$ | $6.4 \pm 1.5$ | 9.4 | 1.08 |
| NGC 4688 ....... | $0.0725 \pm .005$ | $0.0690 \pm 0.003$ | $25.9 \pm 3.2$ | $9.0 \pm 0.8$ | 15 | 1.07 |
| NGC 5474 ....... | $>0.1$ | $0.0576 \pm 0.01$ | $95.4 \pm 6.4$ | $14.9 \pm 0.7$ | 10 | 1.18 |
| NGC 5701 ....... | $0.0322 \pm .01$ | $0.0419 \pm 0.008$ | $43.0 \pm 3.0$ | $4.1 \pm 0.3$ | 3.6 | 1.03 |
| UGC 12732...... | $0.0297 \pm .02$ | $0.0613 \pm 0.009$ | $15.3 \pm 5.7$ | $5.5 \pm 1.4$ | 6.0 | 1.28 |

relation. For instance, HHMRvZ comment that very morphologically disturbed galaxies such as NGC 1637 often have undisturbed H I line profiles.

The morphology of the asymmetries themselves is also worthy of study. KHL classified asymmetric morphology in three categories according to the relative locations of the maximum and minimum flux sectors in the eight-segment R-band analysis. The categories included "bisymmetric," in which the extreme sectors were adjacent, "boxy," in which the extreme sectors were 90° apart, and "lopsided," in which the extreme sectors were 135° or 180° apart. Of the galaxies in this study classified as asymmetric by KHL, NGC 991, UGC 6429, and NGC 5474 were classified as lopsided, while NGC 1042, 3596, and 4688 were classified as boxy. We find that in H I, all of these galaxies exhibit lopsided asymmetry, except for NGC 1042. NGC 1042 exhibits boxy asymmetry, caused by the peculiar perpendicularity of its morphological and dynamical major axes. The remaining galaxies in the current sample were classified as symmetric by KHL and therefore were not categorized in this way in the R band. Of these galaxies, NGC 5701 and UGC 3685 are boxy in the H I, while UGC 12732 is lopsided. None of the observed galaxies were "bisymmetric" in the H I.

It is also of interest to search for asymmetry trends as a function of global gas parameters. Figure 13 illustrates the relationships between $A_{f,\mathrm{H\,I}}$ and the relevant global H I parameters of the targets as listed in Table 3. Again, no clear relationships are apparent. The relationship between dynamical asymmetry and global H I properties is even more tenuous. Figure 14 illustrates this clearly. There are no detectable dependencies of any global property of the gas on the rotation asymmetry $S_2$.

### 3.2. Comparison of Current Techniques

As discussed in § 1, several studies of optical morphological asymmetry have been conducted, in general using a number of different quantitative measures. One of these, that by Conselice, Bershady, & Jangren (2000b), includes NGC 3596 and NGC 5701 in its galaxy sample. They employ a method in which a galaxy image is rotated through some angle $\phi$ and then is subtracted from the original, unrotated image. The normalized residuals are taken as the asymmetry measurement. Our measure of R-band morphology is in disagreement with Conselice et al. (2000b), insofar as NGC 3596 is one of our most symmetric galaxies as measured by $A_{f,R}$, and NGC 5701 is measured to have moderate asymmetry by the same quantifier. In contrast, Conselice et al. (2000b) find that NGC 3596 is more asymmetric than about 75% of their sample, and NGC 5701 is one of the most symmetric. These differences are likely due to several factors; primarily, our methods are fundamentally different and measure different types of asymmetry. In addition, centering issues are very likely to be an important factor in the disagreement here, as Conselice et al. (2000b) use a different centering method from that used here (see below).

The dynamical symmetry properties that we have derived represent a wide range of dynamical variables, so that the combination of these parameters allows for the study of the global properties of a galaxy that are the most easily accessible to the casual observer. Other techniques for the determination of dynamic asymmetry have also been proposed, such as that by SFdZ. These authors present methods by

which lopsided spiral modes and global elongation in the galactic potential may be inferred from the presence of nonaxisymmetric motions in the observed velocity field. In light of theoretical models such as that of Jog (1997), it is clear that perturbations in the gravitational potential can manifest as perturbations in the observed velocity fields.

Unlike the work presented here, determining the spiral structure of the potentials of disk galaxies using the method of SFdZ leads immediately to information about the total mass distribution in galactic halos. Nevertheless, the method is complex and is most applicable over a narrow range of inclinations. The parameters calculated in the present work are calculable over a wide range of galaxy inclinations and are quickly attainable from basic data, and thus they are better suited to identifying asymmetric galaxies quickly from large samples. Once identified, more detailed methods would be invaluable for deriving the perturbed galactic potential of individual galaxies.

A method based on SFdZ was used by S3vA to quantify the asymmetry in the two galaxies presented in that paper, NGC 4395 and DDO 9. They find that both galaxies, selected for strong kinematic lopsidedness, exhibit asymmetric rotation curves. To test this observation, we attempted to apply the SFdZ method to our sample of nine galaxies to find the zeroth through third harmonic components of each galaxy's velocity field as a function of radius. However, because of the low inclinations of these galaxies, satisfactory decomposition into harmonic kinematic components for the comparison was impossible, as measured in part by consistently large values of the third cosine coefficient, $\hat{c}_3$, which should be zero when the inclination of the tilted-ring fit is correct.

Closely connected with the present method and those of Conselice et al. (2000b), SFdZ, and others is the question of centering. Although not yet utilized as a parameter of asymmetry itself, the question of finding the kinematic center and/or the center of light of a galaxy is critical to the question of galactic symmetry; imprecise determination of the center of the galaxy can easily introduce unacceptable errors in the determination of symmetry properties. In the present method and that of Conselice et al. (2000b), improper centering creates a false dipole in the overlay pattern (or the rotation) for determining morphology, as it does for true Fourier morphology techniques, such as that of Zaritsky & Rix (1997). Improper centering also contaminates measures of $S_2$ and $\Delta\Gamma$. In this work, centers for kinematic parameters were chosen iteratively for best $\chi^2$ fit in the tilted-ring model, while the centers for the morphological parameters were chosen as the centers of light of the optical galaxy. Conselice et al. (2000b) iteratively find the centering that minimizes their morphological asymmetry parameter. SFdZ recommend selecting centers that minimize the total residual velocity.

Beauvais & Bothun (1999) also consider the issue of centering when applying a tilted-ring model to Fabry-Perot data. They use three methods for centering the galaxy: photometric ellipse fitting, finding the center of symmetry of the tilted-ring model, and fitting the center as a free parameter in the tilted-ring model. They report that each of these centering methods yielded equally good model velocity fields, but that it was common for the center to vary considerably in the outer radii of the galaxy when allowed to vary freely, and they interpret this as possibly indicating actual misalignment of the inner and outer rotation axes.

Because centering is so critical, nearly all studies of asymmetry must choose one or two methods for finding the center of a galaxy. These derived centers themselves can also be used as indicators of lopsidedness. Offsets of the kinematic center from the optical center of light and dependence on the derived kinematic center on radius can both be indicators of lopsided dynamics. In this work, the sample galaxies were chosen on the basis of their face-on inclinations for the purpose of examining the optical morphology, making the kinematic centers not sufficiently certain for comparison with morphological centers. However, future work with more inclined galaxies may be able to use centering itself as a symmetry indicator.

## 4. SUMMARY

This work represents a concurrent analysis of both optical and 21 cm symmetry properties of a sample of disk galaxies. We have presented methods by which the symmetry properties of a galaxy can be quickly computed over a wide range of dynamic variables. These parameters are sensitive to both noncircular and nonplanar motions, depending in large part on the inclinations of the galaxies. In this case, the face-on inclinations of the targets make the parameters most sensitive to nonplanar motions.

In our sample presented here, tidal interaction with companion objects dominates the asymmetry in NGC 5474 and cannot be ruled out for NGC 1042 and NGC 4688. Nevertheless, dynamical nonaxisymmetries clearly prosper in more isolated and even morphologically symmetric galaxies such as UGC 12732 and UGC 3685 as well. Pervasive deviations from axisymmetry even outside tidal interactions seem to indicate that asymmetric galaxies are stable and long-lived phenomena. Our data seem, however, to indicate that there is little or no connection between lopsided morphology and nonplanar motions in such galaxies. This lack of clear connection between morphology and warping seems to imply that separate physical mechanisms may be at work in each domain to produce deviations from flat, axisymmetric disks.

The methods presented in this paper can be quickly applied to large samples of galaxies to identify deviations from axisymmetry in dynamics and morphology. The small sample size of this initial study and the kinematic uncertainties produced by the sample galaxies' face-on inclinations can rule out only the strongest of correlations among the various parameters. Larger samples and samples at varying inclinations are required to study the true relationships between these parameters at more than a cursory level. A future study with galaxies of a wider range of inclinations will also allow for additional parameters such as kinematic offsets, which can then be adequately studied. Future numerical work can also benefit from an easily applied method to track and identify departures from symmetry. Such numerical work could, for instance, study the origins and longevity of asymmetries and predict the course of their evolution in spiral galaxies.

## REFERENCES

Baldwin, J. E., Lynden-Bell, D., & Sancisi, R. 1980, MNRAS, 193, 313
Beauvais, C., & Bothun, G. 1999, ApJS, 125, 99
Begeman, K. G. 1989, A&A, 223, 47
Bottinelli, L., Gouguenheim, L., Paturel, G., & de Vaucouleurs, G. 1985, A&AS, 59, 43
Buta, R., van Driel, W., Braine, J., Combes, F., Wakamatsu, K., Sofue, Y., & Tomita, A. 1995, ApJ, 450, 593
Condon, J. J., Cotton, W. D., Greisen, E. W., Yin, Q. F., Perley, R. A., Taylor, G. B., & Broderick, J. J. 1998, AJ, 115, 1693
Conselice, C. J., Bershady, M. A., & Gallagher, J. S., III. 2000a, A&A, 354, 21
Conselice, C. J., Bershady, M. A., & Jangren, A. 2000b, ApJ, 529, 886
Cornwell, T. J., Uson, J. M., & Haddad, N. 1992, A&A, 258, 583
Dekel, A., & Shlosman, I. 1983, in IAU Symp. 100, Internal Kinematics and Dynamics of Galaxies, ed. E. Athanassoula (Dordrecht: Reidel), 187
de Vaucouleurs, G., de Vaucouleurs, A., Corwin, H. G., Buta, R. J., Paturel, G., & Foqué, P. 1991, Third Reference Catalogue of Bright Galaxies (Austin: Univ. Texas Press) (RC3)
DuPrie, K., & Schneider, S. E. 1996, AJ, 112, 937
Fisher, J. R., & Tully, R. B. 1981, ApJS, 47, 139
Garcia, A. M. 1993, A&AS, 100, 47
Gaskell, C. M. 1992, ApJ, 389, 17L
Haynes, M. P., Hogg, D. E., Maddalena, R. J., Roberts, M. S., & van Zee, L. 1998, AJ, 115, 62 (HHMRvZ)
Hewitt, J. N., Haynes, M. P., & Giovanelli, R. 1983, AJ, 88, 272
Huchtmeier, W. K., & Witzel, A. 1979, A&A, 74, 138
Jog, C. J. 1997, ApJ, 488, 642
Kamphuis, J., Sancisi, R., & van der Hulst, T. 1991, A&A, 224, L29
Knapen, J. H. 1997, MNRAS, 286, 403
Kornreich, D. A., Haynes, M. P., & Lovelace, R. V. E. 1998, AJ, 116, 2154 (KHL)
Lasker, B. M., Sturch, C. R., McLean, B. J., Russell, J. L., Jenkner, H., & Shara, M. M. 1992, HST Guide Star Catalog (Baltimore: STScI)
Lovelace, R. V. E., Zhang, L., Kornreich, D. A., & Haynes, M. P. 1999, AJ, 524, 634

Lu, N. Y., Hoffman, G. L., Groff, T., Roos, T., & Lamphier, C. 1993, ApJS, 88, 383
Mould, J., Aaronson, M., & Huchra, J. 1980, ApJ, 238, 458
Napier, P. J., Thompson, R. T., & Ekers, R. D. 1983, Proc. IEEE, 71, 1295
Press, W. H., Flannery, B. P., Teukolsky, S. A., & Vetterling, W. T. 1986, Numerical Recipes in FORTRAN (Cambridge: Cambridge Univ. Press)
Richter, O.-G., & Sancisi, R. 1994, A&A, 290, L9
Rix, H.-W., & Zaritsky, D. 1995, ApJ, 447, 82
Roberts, M. S., & Haynes, M. P. 1994, ARA&A, 32, 115
Rownd, B. K., Dickey, J. M., & Helou, G. 1994, AJ, 108, 1638 (RDH)
Sandage, A., & Tammann, G. 1974, ApJ, 190, 525
Schoenmakers, R. H. M., Franx, M., & de Zeeuw, P. T. 1997, MNRAS, 292, 349 (SFdZ)
Schulman, E., Brinks, E., Bregman, J. N., & Roberts, M. S. 1997, AJ, 113, 1559
Staveley-Smith, L., & Davies, R. D. 1988, MNRAS, 231, 833
Swaters, R. A., Schoenmakers, R. H. M., Sancisi, R., & van Albada, T. S. 1999, MNRAS, 304, 330 (S3vA)
Taga, M., & Iye, M. 1998a, MNRAS, 299, 111
———. 1998b, MNRAS, 299, 1132
Tifft, W. G., & Cocke, W. J. 1988, ApJS, 67, 1
Toomre, A. 1983, in IAU Symposium 100, Internal Kinematics and Dynamics of Galaxies, ed. E. Athanassoula (Dordrecht: Reidel), 177
Tubbs, A. D., & Sanders, R. H. 1979, ApJ, 230, 736
van der Hulst, J. M., & Huchtmeier, W. K. 1979, A&A, 78, 82
van der Hulst, J. M., Terlouw, J. P., Begeman, K., Zwitser, W., & Roelfsema, P. R. 1992, in ASP Conf. Ser. 25, Astronomical Data Analysis and Systems, ed. D. Worall, C. Biemesderfer, & J. Barnes (San Francisco: ASP), 131
van Gorkom, J. H., Knapp, G. R., Raimond, E., Faber, S. M., & Gallagher, J. S. 1986, AJ, 91, 791
Verheijen, M. A. W. 1997, Ph.D. thesis, Univ. Groningen
Weinberg, M. D. 1998, MNRAS, 299, 499
Zaritsky, D., & Rix, H.-W. 1997, ApJ, 477, 118